

# HUBBLE SPACE TELESCOPE SURVEY OF INTERSTELLAR <sup>12</sup>CO/<sup>13</sup>CO IN THE SOLAR NEIGHBORHOOD

Y. SHEFFER<sup>1</sup>, M. ROGERS<sup>1,2</sup>, S. R. FEDERMAN<sup>1</sup>, D. L. LAMBERT<sup>3</sup>, AND R. GREDEL<sup>4</sup>

*Submitted to ApJ: 2007/05/08; Accepted: 2007/06/15*

## ABSTRACT

We examine 20 diffuse and translucent Galactic sight lines and extract the column densities of the <sup>12</sup>CO and <sup>13</sup>CO isotopologues from their ultraviolet A–X absorption bands detected in archival Space Telescope Imaging Spectrograph data with  $\lambda/\Delta\lambda \geq 46,000$ . Five more targets with Goddard High-Resolution Spectrograph data are added to the sample that more than doubles the number of sight lines with published *Hubble Space Telescope* observations of <sup>13</sup>CO. Most sight lines have 12-to-13 isotopic ratios that are not significantly different from the local value of 70 for <sup>12</sup>C/<sup>13</sup>C, which is based on mm-wave observations of rotational lines in emission from CO and H<sub>2</sub>CO inside dense molecular clouds, as well as on results from optical measurements of CH<sup>+</sup>. Five of the 25 sight lines are found to be fractionated toward lower 12-to-13 values, while three sight lines in the sample are fractionated toward higher ratios, signaling the predominance of either isotopic charge exchange or selective photodissociation, respectively. There are no obvious trends of the <sup>12</sup>CO-to-<sup>13</sup>CO ratio with physical conditions such as gas temperature or density, yet <sup>12</sup>CO/<sup>13</sup>CO does vary in a complicated manner with the column density of either CO isotopologue, owing to varying levels of competition between isotopic charge exchange and selective photodissociation in the fractionation of CO. Finally, rotational temperatures of H<sub>2</sub> show that all sight lines with detected amounts of <sup>13</sup>CO pass through gas that is on average colder by 20 K than the gas without <sup>13</sup>CO. This colder gas is also sampled by CN and C<sub>2</sub> molecules, the latter indicating gas kinetic temperatures of only 28 K, enough to facilitate an efficient charge exchange reaction that lowers the value of <sup>12</sup>CO/<sup>13</sup>CO.

*Subject headings:* ISM: abundances — ISM: molecules — ultraviolet: ISM

## 1. INTRODUCTION

Measurements of isotopic ratios in the interstellar medium (ISM) are used to infer the past history of chemical enrichment across the Galaxy. Both quiescent stellar evolution as well as explosive stellar processes are sources of carbon isotopes that enrich the ISM. In our Solar System the carbon isotopic ratio, <sup>12</sup>C/<sup>13</sup>C, is found to be 89 (Anders & Grevesse 1989), thus providing a benchmark value dating back 4.6 billion years to the time of Solar formation. Red giant stars are prodigious converters of <sup>12</sup>C into <sup>13</sup>C, and their ongoing mass loss is a major factor in the continuous lowering of the 12-to-13 ratio in the ISM. For example, observations of CN, CO, and CS in highly-evolved AGB and post-AGB stars show <sup>12</sup>C/<sup>13</sup>C values from 70 down to 30 in photospheric layers and in circumstellar shells that are being injected into the ISM (Lambert et al. 1986; Kahane et al. 1992). Planetary nebulae are later stages of low-mass stellar evolution, showing very low values of <sup>12</sup>CO/<sup>13</sup>CO from 31 down to 2 (Balser et al. 2002), or from 23 down to 9 for the sample in Palla et al. (2000), as well as low 12-to-13 values from observations of C III (Clegg et al. 1997; Palla et al. 2002; Rubin et al. 2004). Thus in the present-day, local ISM we should find <sup>12</sup>C/<sup>13</sup>C values that are between the higher (older) Solar System value and the lowest (youngest) values found in highly-evolved objects.

The 12-to-13 carbon ratio should change not only in time, but also in space. Specifically, it is expected to increase monotonically with Galactocentric distance owing to lower cumulative numbers of star formation generations and <sup>13</sup>C mass loss episodes that have occurred farther from the Galactic center. This picture has been confirmed by ISM studies employing the easily-detected mm-wave emission lines of <sup>12</sup>C- and <sup>13</sup>C-bearing molecules to infer <sup>12</sup>C/<sup>13</sup>C inside dense molecular clouds. Observations of CO (Langer & Penzias 1990) and H<sub>2</sub>CO (Henkel et al. 1982) show that the ratio of the <sup>12</sup>C-bearing molecules to their heavier counterparts are higher in the outer parts of the Galactic disk than in its inner parts—see reviews by Wilson & Rood (1994) and Wilson (1999), as well as the work of Savage et al. (2002) and Milam et al. (2005), who observed mm-wave emission from CN in molecular clouds and derived a Galactic gradient similar to that seen in CO. However, appreciable scatter is found in the measured <sup>12</sup>C/<sup>13</sup>C at each Galactocentric distance, which according to Wilson (1999) is providing evidence for actual source-to-source differences. Averaging isotopic ratios from 13 sources in the local ISM gives  $69 \pm 6$ , while the fit to the Galactic gradient predicts <sup>12</sup>C/<sup>13</sup>C =  $71 \pm 13$  at the solar circle, indicating some 25% enrichment of <sup>13</sup>C relative to <sup>12</sup>C in the ISM over the last 4.6 eons.

<sup>1</sup> Department of Physics and Astronomy, University of Toledo, Toledo, OH 43606; ysheffe@utnet.utoledo.edu, steven.federman@utoledo.edu

<sup>2</sup> Also at Marietta College, Marietta, OH 45750; rogerse@marietta.edu

<sup>3</sup> Astronomy Department, University of Texas, Austin, TX 78712; dll@astro.as.utexas.edu

<sup>4</sup> Max Planck Institut für Astronomie, Königstuhl 17, D-69117 Heidelberg, Germany; gredel@mpia.de

Another molecule used as a proxy for the  $^{12}\text{C}/^{13}\text{C}$  along diffuse and translucent sight lines is  $\text{CH}^+$ , which has been investigated primarily via its optical  $A-X$  transition at 4232.548 Å. After a period of initial confusion, published  $^{12}\text{CH}^+ / ^{13}\text{CH}^+$  values eventually settled around an average value near 70 [e.g., Crane et al. (1991), Stahl & Wilson (1992), Hawkins et al. (1993)], confirming that  $\text{CH}^+$  is not susceptible to fractionation because its formation occurs via non-thermal processes. Thus  $\text{CH}^+$  provides confirmation that the Wilson (1999) average of  $69 \pm 6$  from mm-wave emission data of dense molecular cloud cores is a good indicator of  $^{12}\text{C}/^{13}\text{C}$  in the local ISM. We shall, therefore, take the ambient value of  $^{12}\text{C}/^{13}\text{C}$  in the solar neighborhood to be  $70 \pm 7$ .

Besides mm-wave probing of dense clouds and  $\text{CH}^+$  in much more tenuous lines of sight, there are other cases that confirm the ambient carbon isotopic ratio of 70. In the vacuum UV (VUV), Sheffer et al. (2002b) reported  $^{12}\text{CO}/^{13}\text{CO} = 73 \pm 12$  toward X Per (HD 24534), albeit with highly fractionated  $\text{C}^{16}\text{O}/\text{C}^{18}\text{O}$  and  $\text{C}^{16}\text{O}/\text{C}^{17}\text{O}$  values. Burgh et al. (2007) reported 12-to-13 CO ratios for six sight lines, five of which resulted in values that were consistent with 70 to within  $2\sigma$ . Six out of seven  $^{13}\text{CO}$  sight lines in the sample of Sonnentrucker et al. (2007) are consistent with unfractionated CO at the same level of significance. In the near infrared (NIR), toward the dense cloud AFGL 490, Goto et al. (2003) derived  $^{12}\text{CO}/^{13}\text{CO} = 86 \pm 49$ , i.e., indistinguishable from the ambient carbon ratio. The sight line toward the massive protostar NGC 7538 IRS9 provided the first isotopic measurement of solid CO in the ISM. NIR data presented in Boogert et al. (2002) show that the ratio of  $^{12}\text{CO}$  ice to  $^{13}\text{CO}$  ice is  $71 \pm 5$ . Moreover, this agreement is also displayed by ices of another C-bearing molecule, since  $^{12}\text{CO}_2 / ^{13}\text{CO}_2 = 80 \pm 11$  along the same line of sight (Boogert et al. 2000).

As the examples above show, most isotopic carbon ratios are inferred from C-bearing molecular proxies, especially CO, thanks to the larger isotopic shifts that are encountered in molecules. However, in the ISM, carbon isotopic ratios that are derived via molecular proxies are sometimes found to be fractionated. Two opposing effects are usually invoked to explain CO fractionation away from the ambient  $^{12}\text{C}/^{13}\text{C}$ . An isotopic charge exchange (ICE) reaction  $^{13}\text{C}^+ + ^{12}\text{CO} \rightarrow ^{12}\text{C}^+ + ^{13}\text{CO} + 35\text{ K}$  (Watson et al. 1976) works to lower the  $^{12}\text{CO}$ -to- $^{13}\text{CO}$  ratio when a lower gas temperature and a high  $\text{C}^+$  abundance are present, while selective photodissociation (SPD) in ultraviolet (UV) photon-dominated regions drives the ratio higher through self shielding by the more abundant isotopologue, i.e.,  $^{12}\text{CO}$  (Bally & Langer 1982; van Dishoeck & Black 1988). Deep inside dark molecular clouds no fractionation of CO is expected because of the absence of both ionized carbon and UV photons.

In order to explore how well  $^{12}\text{CO}/^{13}\text{CO}$  in diffuse molecular clouds reflects the underlying 12-to-13 carbon ratio, we study its fractionation processes here in more detail through a larger sample of sight lines. It is important to verify that the 12-to-13 variations are source-related and not induced by systematic effects such as noise and modeling uncertainties. Therefore, because the treatment of absorption along an infinitesimal beam is significantly less complicated than that of emission from a finite volume, and since the Space Telescope Imaging Spectrograph (STIS) records high-quality spectra of a large number of saturated as well as optically-thin CO bands per sight line, we are able to provide evidence for source-to-source variation in  $^{12}\text{CO}/^{13}\text{CO}$ , and consider photochemical fractionation as its cause.

## 2. DATA, REDUCTION, AND SPECTRUM SYNTHESIS

Our sample includes 20 stars observed with STIS at resolving power ( $R$ ) between 46,000 (grating E140M) and 160,000 (grating E140H) and five stars that have *Hubble Space Telescope* (HST) data from its Goddard High-Resolution Spectrograph (GHRS). Although  $R$  of the GHRS grating G160M is the lowest in the current sample (19,000), with proper sampling of weak and strong bands and with high enough signal-to-noise ratio (S/N), the data are very useful for robust modeling of CO column densities. This was nicely demonstrated by Lambert et al. (1994) who presented G160M data for  $\zeta$  Oph having  $\text{S/N} \sim 900(!)$  and by Federman et al. (2003), who modeled CO toward  $\rho$  Oph A and  $\chi$  Oph using G160M data with  $\text{S/N} \sim 200$ . These three stars were added to the sample, as well as HD 96675 and HD 154368, which have GHRS spectra with only moderate S/N; the results of their low- $R$  CO modeling are less secure than for the rest of the sample.

Table 1 lists all 25 sight lines and gives stellar spectral types, apparent  $V$  magnitudes, Galactic coordinates, velocity corrections to the Local Standard of Rest (LSR), reddening values, and heliocentric and Galactocentric distances. The farthest target examined here is HD 177989, which lies 5 kpc away. Table 2 provides a listing of STIS and GHRS data sets that were used in our analysis. Also listed for each data set are grating and aperture used, S/N achieved, and  $R$ , derived as a fitted parameter during CO spectral syntheses. Whenever repeated multiple exposures were available, they were combined in wavelength space for improved S/N. In addition, when a feature (band) appeared in two adjacent orders, they were combined after correcting for any small wavelength inconsistencies. All reductions here were performed in IRAF<sup>1</sup> and STSDAS.<sup>2</sup>

All profile syntheses of CO, as well as of  $\text{H}_2$  from spectra acquired with the *Far Ultraviolet Spectroscopy Explorer* (FUSE), were carried out by Y. S. with his simplex Fortran code, Ismod.f. For the determination of CO column density ( $N$ ) we used oscillator strengths ( $f$ -values) for the  $A-X$  bands from Chan et al. (1993), see also Morton & Noreau (1994), which in a global sense have been verified to a level of a few percent by Eidelsberg et al. (1999). Simultaneous multi-parametric profile syntheses of all detected CO bands for each sight line were employed in deriving  $N(^{12}\text{CO})$ ,

<sup>1</sup> IRAF is distributed by the National Optical Astronomical Observatory, which is operated by the Association of Universities for Research in Astronomy, Inc., under cooperative agreement with the National Science Foundation.

<sup>2</sup> STSDAS is a product of the Space Telescope Science Institute, which operated by AURA for NASA.

$N(^{13}\text{CO})$ , and excitation temperatures ( $T_{\text{ex}}$ ), as well as observed radial velocity and fitted equivalent width ( $W_\lambda$ ) for each band. Cloud component structures from high- $R$  optical observations of CH  $\lambda 4300$  were available for 19 of the 22 sight lines analyzed here, but relative fractions and  $b$ -values of all components were allowed to vary (i.e., only velocity differences were left fixed during the fit). The remaining three cases without available CH component structures happen to be the sight lines with the lowest amounts of detected CO, thus affording uncomplicated abundance determinations. Detailed cloud structures and model results for CH and  $\text{H}_2$  will appear elsewhere. Here, values for  $N_{\text{tot}}$  of  $\text{H}_2$  and its excitation temperatures  $T_{1,0}$  and  $T_{4,0}$  will be quoted and analyzed.

The important aspect of correctly handling any effects of line saturation was realized by including both very weak  $A-X$  bands with optical depth at line center of  $\sim 1$  or less, which are sensitive mostly to the total CO column density, as well as very strong  $A-X$  bands having  $f$ -values many times larger, which dictate how the cloud components should be modeled. Figures 1 and 2 show two examples of multi-band fits toward HD 208266 of  $^{12}\text{CO}$  and  $^{13}\text{CO}$ , respectively. The wide spectral coverage and the high abundance of CO along this sight line combine to give us the highest practical number (14) of usable absorption bands for  $^{12}\text{CO}$ , as well as seven consecutive bands of  $^{13}\text{CO}$ . In terms of optical depth ( $\tau$ ), the model of  $^{12}\text{CO}$  shows that  $\tau$  increases by a factor of 1150 from  $A-X$  (13-0) to  $A-X$  (2-0), whereas  $\tau$  of the  $^{13}\text{CO}$  bands varies by a factor of 20. It should be noted that a full-scale fit of 14  $A-X$  bands involves simultaneous modeling of the column density in 126 VUV transitions of CO, when the model includes three parametrized excitation temperatures, or nine rotational transitions, per band. This large number of modeled lines is what makes such a global fit very robust, even when the data (from E140M) have moderate  $R$  and S/N.

Some details from these spectral fits, as well as model  $N$  values, are given in Table 3 for  $^{12}\text{CO}$  and in Table 4 for  $^{13}\text{CO}$ . Results are listed for the two  $A-X$  bands (denoted by  $v'$ ) that straddle the  $\tau = 1$  condition at the center of the R(0) line. These results include fitted  $W_\lambda$ , optical depth, and column density. The two bands are then used to infer the uncertainty on the derived column density by averaging their relative uncertainties in equivalent width and by assuming that the result is identical to the relative error in the column density. Of course, the lower the optical depth, the better is this assumption. However, one cannot use absorption bands that are too weak ( $\tau \ll 1$ ), because of the increasing influence of the noise relative to the decreasing signal from CO.

The modeling methodology was to derive a cloud structure for the  $^{12}\text{CO}$  molecule, and then to apply it as a fixed structure during modeling of  $^{13}\text{CO}$ . The number of components, their relative fractions, and their velocity separations were all kept fixed, under the assumption that the two isotopologues reside in the same clumps of gas, with all components having identical 12-to-13 ratios for a given sight line. This assumption is kinematically verified, since the radial velocities of both species in our sample agree very well with each other. This agreement is shown in Fig. 3, a plot of the difference  $V_{\text{helio}}(^{13}\text{CO}) - V_{\text{helio}}(^{12}\text{CO})$  against the heliocentric radial velocity scale of  $^{12}\text{CO}$ . With an average of  $-0.2 \pm 0.4 \text{ km s}^{-1}$ , the scatter in this sample is consistent with a vanishing radial velocity difference between the two isotopologues. The  $1\sigma$  velocity dispersion of  $0.4 \text{ km s}^{-1}$  is a small fraction of the resolution element for the data, being  $0.22\Delta\lambda$  and  $0.06\Delta\lambda$  for E140H and E140M, respectively.

Although it is known that the STIS line spread function (LSF) possesses weak wings (see the STIS handbook), we could not see any obvious signatures for such wings in the highest- $R$  data. Therefore, a single Gaussian was used to describe the instrumental profile of STIS. This is in agreement with the findings of Jenkins & Tripp (2002), who analyzed the unbinned (but noisier and lacking proper flat-fielding) raw spectral data. Nevertheless, the STIS handbook does show that the LSF wings have a larger role in the profile for wider slits. Therefore,  $R$  was treated as a fittable parameter during modeling, and it is apparent that  $R$  is lower for E140H data taken through wider slits (see Fig. 4). There is a good match between the range of  $R$  found here and the range found by Bowers (1998) for the 0'09 slit, as well as his listed range for the smallest ("Jenkins") slit based on ground (pre-launch) measurements. Furthermore, our tests show that a 15% error in  $R$  affects the derived column density by only  $\sim 6\%$ . Since both  $N(^{12}\text{CO})$  and  $N(^{13}\text{CO})$  vary similarly in response to any  $R$  change, derived isotopic ratios are affected at a level of  $\lesssim 3\%$  according to these tests.

The trend of lower  $R$  with larger slit width is not limited to the E140H grating, as shown by modeling medium- $R$  data from the E140M grating. Three sight lines return an average of  $R = 45,600 \pm 1,000$  for the 0'06 slit, in excellent agreement with the value 46,000 given in Bowers (1998). On the other hand, a couple of sight lines were observed through the wider 0'2 slit, and their fitted  $R$  values are 38,000 and 39,000, i.e., clearly corroborating the trend of decreasing  $R$  with larger slit widths.

### 3. COMPARISON WITH PREVIOUS RESULTS

#### 3.1. Internal Comparison with Previous Ismod.f Results

The results presented in this paper reflect simultaneous modeling of all detectable  $A-X$  bands per sight line, but initial Ismod.f fits of certain sight lines did not use all available bands. It is of interest to compare the latest and most extensive fits with less ambitious initial modeling to learn about the dependence of model results on the number of bands being fitted simultaneously. Sheffer et al. (2002a) modeled a four-component cloud structure of  $N(^{12}\text{CO})$  and  $N(^{13}\text{CO})$  toward HD 24534 using the strongest and weakest of only seven  $A-X$  bands that were available from the STIS o648o12-13 data sets, as well as any available intersystem bands. For comparison and completeness, we obtained and analyzed the STIS o66p01-2 data sets from the *HST* archive and modeled a total of 12  $A-X$  bands toward X Per, using all four E140H data sets. Keeping a four-component cloud model, the fit returned  $N(^{12}\text{CO}) = (1.58 \pm 0.04) \times 10^{16} \text{ cm}^{-2}$ , which is 12% higher than the value in Sheffer et al. (2002a).

However, re-synthesizing the  $^{13}\text{CO}$  bands toward X Per returned a new column density of  $1.55 \times 10^{14} \text{ cm}^{-2}$ , which

was lower by 20% than the Sheffer et al. (2002a) value. This newer fit was based on 9 bands covering a robust range of optical depth and  $f$ -values. A closer inspection revealed that the weaker bands were not being fitted correctly, showing as excess of observed absorption relative to the model. We, therefore, relaxed the usual method of keeping the component structure that was derived from  $^{12}\text{CO}$  fixed during  $^{13}\text{CO}$  fits, by allowing the  $b$ -values to vary during the synthesis. This resulted in a better fit to the data, yielding a larger  $N(^{13}\text{CO})$ , albeit 4% below the value in Sheffer et al. (2002a). Thus our published value ( $73 \pm 12$ ) for  $^{12}\text{CO}/^{13}\text{CO}$  is updated here to  $85 \pm 5$ , or higher by  $1.0 \sigma$ . Since more bands were used in the latest fit, its results should be more secure than before. The combination of high CO column density,  $N(^{12}\text{CO}) \geq 10^{16} \text{ cm}^{-2}$  and  $N(^{13}\text{CO}) > 10^{14} \text{ cm}^{-2}$ , and high S/N in observed low- $v'$  (stronger) bands of  $^{13}\text{CO}$ , is what allowed us to detect the anomaly in the first place and then to treat it. Both  $^{12}\text{CO}$  and  $^{13}\text{CO}$  are still assumed to reside in the same clumps of gas, albeit with different line widths. Another option, that of allowing a fit of cloud component fractions, would have explored a new territory of variable isotopic ratios among clumps of gas, which we decided not to pursue at the present time.

Toward HD 203374A, we previously published two  $N(^{12}\text{CO})$  values based on the five  $A-X$  bands (7–0) through (11–0) from the E140H data set, together with the  $C-X$  (0–0) band from lower- $R$  *FUSE* data, which provided the high- $\tau$  leverage for the Ismod.f synthesis (Sheffer, Federman, Pan, & Andersson 2003; Pan et al. 2005). Here, the much more extensive set of bands available in the E140M (lower- $R$ ) data set was analyzed. A simultaneous fit of 112 transitions in 13  $A-X$  bands, (0–0) through (12–0), returned a value for  $N(^{12}\text{CO})$  only 6% higher than Sheffer, Federman, Pan, & Andersson (2003), or a value that agrees perfectly with Pan et al. (2005). This good agreement demonstrates that one need not resort to the highest- $R$  available (e.g., through E140H) as long as there is an adequate and robust coverage of many bands from medium- $R$  (E140M) exposures.

### 3.2. Comparison with Previous External Results

Since relatively little has been done concerning UV data on  $^{13}\text{CO}$  in the past, most of the common sight lines involve comparisons of  $^{12}\text{CO}$  results (see Table 5). Previously published  $^{13}\text{CO}$  sight lines with *HST* observations include  $\zeta$  Oph (Sheffer et al. 1992; Lambert et al. 1994), X Per (Sheffer et al. 2002a), and  $\rho$  Oph A and  $\chi$  Oph (Federman et al. 2003), all modeled with Ismod.f. Two recent studies by Burgh et al. (2007) and Sonnentrucker et al. (2007) investigated  $^{12}\text{CO}$ ,  $^{13}\text{CO}$ , and  $\text{H}_2$  along diffuse and translucent sight lines. Lines of sight with detections of  $^{13}\text{CO}$  in the two studies amounted to 6/23 and 7/10 of the whole samples, respectively, of which four targets were common to both. Together, these two studies introduced six sight lines with previously unpublished *HST* data for  $^{13}\text{CO}$ : HD 27778, HD 177989, HD 203532, HD 206267, HD 207198, HD 210121, and HD 210839. The current sample presents independent data reduction and analysis of 22  $^{13}\text{CO}$  sight lines, of which 15 have no previously published  $^{12}\text{CO}$ -to- $^{13}\text{CO}$  results, bringing the total number of sight lines with detectable  $^{13}\text{CO}$  based on *HST* data from 11 to 26.

Burgh et al. (2007) modeled their data with a single cloud component, resulting in a single “effective”  $b$ -value for all their sight lines. Furthermore, instead of using a self-fitting code, Burgh et al. (2007) created a grid of models and then chose the values of  $N$ ,  $T_{\text{rot}}$ , and  $b$  that best described the data. On the other hand, Sonnentrucker et al. (2007) incorporated a profile-fitting code with multi-component cloud structures from high- $R$  optical spectra of CH and CN, much like our usual method of analysis. We are convinced that the latter methodology results in more realistic characterization of each line of sight, as is evidenced from the overall larger uncertainties associated with the results of Burgh et al. (2007). Both Burgh et al. (2007) and Sonnentrucker et al. (2007) employed the CO  $f$ -values listed in Morton & Noreau (1994), which are the values from Chan et al. (1993). Thus no re-scaling was needed for this comparison with our results, which are also based on the same set of  $f$ -values. Only a single star from Sonnentrucker et al. (2007) (HD 210121) is not included in the current sample because there is a very limited coverage by GHRS exposures. By not including literature results our entire sample is kept as homogeneous as possible in terms of data reduction, measurements, and Ismod.f spectrum synthesis fits. Table 5 shows that  $^{12}\text{CO}/^{13}\text{CO}$  results for the seven common sight lines are in agreement to within  $1.5 \sigma$ , with the sole exception of the Kaczmarczyk (2000) value for X Per owing to improper input cloud structure during modeling (Sheffer et al. 2002a).

## 4. ISOTOPIC RESULTS AND ANALYSIS

### 4.1. $^{12}\text{CO}/^{13}\text{CO}$ Sample

Figure 5 shows  $\log N(^{13}\text{CO})$  versus  $\log N(^{12}\text{CO})$  for all sight lines. The slope corresponding to  $^{12}\text{C}/^{13}\text{C} = 70$  is shown, together with its  $1 \sigma$  range, as well as the slopes of 0.5 and 2.0 times the ratio of 70. The values of  $^{12}\text{CO}/^{13}\text{CO}$  are seen to be centered along the line  $^{12}\text{C}/^{13}\text{C} = 70$ , showing considerable scatter but mostly within the factor-of-2 range relative to 70, i.e., within 35 to 140.

Another view is provided by Fig. 6, which shows a histogram of the current VUV  $^{12}\text{CO}/^{13}\text{CO}$  values, as well as distributions via other detection methods and of other C-bearing molecules. This VUV sample of CO ratios is at the bottom, showing a distribution that is centered near the ambient carbon isotopic ratio (70) with roughly equal numbers of sight lines having lower or higher values. Table 6 shows that  $^{12}\text{CO}/^{13}\text{CO}$  in diffuse molecular clouds varies between  $37 \pm 8$  and  $167 \pm 25$ , a factor of  $4.5 \pm 1.2$ . The almost symmetric distribution is betrayed by 11 sight lines with 12-to-13 ratios below 70 and by 14 sight lines with values above 70. Six UV sight lines, all common with this sample, were analyzed by Burgh et al. (2007) and yielded  $^{12}\text{CO}/^{13}\text{CO}$  values over a narrow range of  $49 \pm 15$  to  $68 \pm 31$ . For a more proper comparison, the same six targets here returned values between  $41 \pm 7$  and  $85 \pm 5$ , in very good agreement with Burgh et al. (2007). However, the sample of Burgh et al. (2007) is dominated by larger 12-to-13 uncertainties

that obscure any possible source-to-source variations, whereas here we are able to discern source-to-source variations thanks to smaller measurement and modeling uncertainties. Another sample of six UV sight lines from *HST* data in Sonnentrucker et al. (2007) shows CO isotopic values between  $46 \pm 6$  and  $79 \pm 12$  for five sight lines common with this sample, from which the range is between  $42 \pm 9$  and  $85 \pm 5$ , revealing very good agreement as well.

Table 6 also lists the isotopic ratios normalized by the carbon ratio, or

$$F_{13} \equiv \frac{^{12}\text{CO}/^{13}\text{CO}}{^{12}\text{C}/^{13}\text{C}} = \frac{^{12}\text{CO}/^{13}\text{CO}}{70}.$$

In terms of  $F_{13}$ , CO isotopic values are found between 0.5 and 2.4, yet very well centered on the ambient carbon isotopic value, or  $F_{13} = 1$ . This distribution is consistent with  $^{12}\text{C}/^{13}\text{C}$  being the “parental” distribution for the CO isotopic ratios. Theoretical models (van Dishoeck & Black 1988) predict ambient isotopic CO ratios for diffuse clouds, and variable ratios that respond to the changing UV flux along a path into a more opaque cloud. Yet the same models fail to predict the observed column densities of CO along diffuse sight lines. Better correspondence may occur once new measurements of  $f$ -values of Rydberg transitions of CO (§ 4.4) are incorporated by such modeling efforts.

#### 4.2. Sight Lines with Fractionated CO

An examination of CO isotopic deviations from 70 shows that 14/25 of sight lines agree with the value of ambient  $^{12}\text{C}/^{13}\text{C}$  at the level of  $\leq 1 \sigma$ , and that three more sight lines agree with the unfractionated value to within  $2 \sigma$ . Thus 32% of sight lines have values of  $^{12}\text{CO}/^{13}\text{CO}$  that are significantly ( $\geq 3 \sigma$ ) different from the carbon isotopic value. Out of these eight sight lines, three have CO that is fractionated upward: X Per =  $85 \pm 5$ ,  $\zeta$  Per =  $108 \pm 5$ , and  $\zeta$  Oph =  $167 \pm 25$  (in order of increasing  $F_{13}$ ), presumably owing to more effective self shielding of  $^{12}\text{CO}$  against photodissociation. The five other sight lines in order of decreasing  $F_{13}$  are: HD 207538 =  $51 \pm 6$ , HD 207198 =  $48 \pm 8$ , HD 206267 =  $42 \pm 9$ , HD 203532 =  $41 \pm 7$ , and HD 154368 =  $37 \pm 8$ . These exhibit fractionation in  $^{13}\text{CO}$ , presumably owing to a larger role of the ICE reaction with  $\text{C}^+$  that enhances the relative abundance of  $^{13}\text{CO}$ . Sonnentrucker et al. (2007) also found CO fractionated toward HD 206267, with  $^{12}\text{CO}/^{13}\text{CO} = 46 \pm 6$ .

The first 12-to-13 VUV study of CO based solely on *HST* data was provided by Lambert et al. (1994), who found  $^{12}\text{CO}/^{13}\text{CO}$  to be  $167 \pm 25$  toward  $\zeta$  Oph. [Previously, Sheffer et al. (1992) derived a 12-to-13 ratio of  $150 \pm 27$  along the same sight line using GHRS data and IUE results.] Furthermore, two more sight lines in Ophiuchus did indicate high UV ratios as reported by Federman et al. (2003), who found 12-to-13 ratios of  $125 \pm 23$  toward  $\rho$  Oph A and  $117 \pm 35$  toward  $\chi$  Oph. When such initial UV reports of highly fractionated CO came out they seemed to be extraordinary. Now the present distribution serves to show that nothing extraordinary is happening even along the line of sight toward  $\zeta$  Oph. Although it still shows the highest  $^{12}\text{CO}$  fractionation (factor of  $2.4 \pm 0.4$ ), another sight line, that of HD 154368, has  $^{13}\text{CO}$  fractionated to the greatest extent of  $1.9 \pm 0.4$ , while six other sight lines were listed above as fractionated to lesser degrees. Thus UV data toward diffuse/translucent sight lines is showing that relative to the local isotopic ratio of carbon, CO can be fractionated upward or downward by a factor of  $\lesssim 2$ . For translucent sight lines, van Dishoeck & Black (1988) models can easily duplicate downward, but not upward, fractionations by about 2, showing the need to improve upon self shielding computations for  $^{12}\text{CO}$ .

We now explore possible relationships between the observed values of  $^{12}\text{CO}/^{13}\text{CO}$  and the other observables that characterize the ISM. This may provide insight into the required combination of parameters that control the observed distribution of the CO isotopic ratio.

#### 4.3. Variation of $^{12}\text{CO}/^{13}\text{CO}$ with CO Column Density

Figure 7 (filled circles) shows the 12-to-13 CO isotopic ratio versus  $N(^{12}\text{CO})$ . The global sense of the plot shows variations in the values of  $^{12}\text{CO}/^{13}\text{CO}$  for different  $N(^{12}\text{CO})$  regimes. [Similar variations are seen when  $^{12}\text{CO}/^{13}\text{CO}$  is plotted against  $N(^{13}\text{CO})$ .] Higher values of the isotopic ratio (above 70) are seen for the lowest column densities, or for the regime of  $N(^{12}\text{CO}) \lesssim 2 \times 10^{15} \text{ cm}^{-2}$ . The second regime is found for  $N(^{12}\text{CO}) \lesssim 6 \times 10^{15} \text{ cm}^{-2}$ , where a significant number of sight lines is found with low 12-to-13 values down to about 50, mixed with sight lines that still show isotopic values higher than 70. Both of these regimes are influenced by UV-dominated photochemistry. The higher values correspond to enhanced photodissociation of  $^{13}\text{CO}$ .  $^{12}\text{CO}$  is already optically thick enough to be self-shielded against UV photodissociation, since according to the self-shielding models of van Dishoeck & Black (1988), the photodissociation rate of CO is diminished by a factor of  $\approx e^{-1}$  once the column density of  $^{12}\text{CO}$  has reached the value of  $\approx 10^{15} \text{ cm}^{-2}$ . Moreover, taking into account the extra shielding from  $\text{H}_2$  spectral features, the shielding of  $^{12}\text{CO}$  commences at lower values,  $N \leq 10^{14.5} \text{ cm}^{-2}$ . The regime that includes low  $^{12}\text{CO}/^{13}\text{CO}$  values probably corresponds to the ICE reaction with  $\text{C}^+$ , which works to increase the abundance of  $^{13}\text{CO}$  at the expense of  $^{12}\text{CO}$  (Watson et al. 1976). Here, UV radiation is needed to ionize C atoms. Finally, at sufficiently high column densities of  $^{12}\text{CO}$ , the third regime in the plot shows mostly unfractionated isotopic ratios, i.e., values that are consistent with  $^{12}\text{C}/^{13}\text{C} = 70$ . In this regime,  $^{13}\text{CO}$  has become mutually shielded by  $^{12}\text{CO}$  (van Dishoeck & Black 1988).

Also shown in Fig. 7 (empty circles) are  $^{12}\text{CO}/^{13}\text{CO}$  determination from Liszt & Lucas (1998), based on mm-wave absorption observations, which show some overlap with VUV results in the middle regime described above, i.e., where low 12-to-13 values are thought to be strongly influenced by ICE. But toward the third regime of highest  $N(^{12}\text{CO})$  values, the mm-wave absorption results are significantly lower than VUV results, signaling that the two are drawn from different populations of sight lines, with the radio observations probably probing much colder gas.

Qualitatively, there is an interesting resemblance between this plot and the solid line in Fig. 11 of van Dishoeck & Black (1988), which models the variation of  $^{13}\text{CO}/^{12}\text{CO}$  as function of depth into a cloud, provided the solid line is inverted to reflect  $^{12}\text{CO}/^{13}\text{CO}$  variations instead. Figure 7 may be interpreted the same way, since  $N(^{12}\text{CO})$  of the abscissa registers the amount of material along the line of sight (increasing optical depth), which can also stand for the amount of molecular material along a path into a cloud.

#### 4.4. Fractionated Values and Their Genesis

We surmise that all CO isotopic ratios would equal  $\sim 70$ , were it not for ICE or SPD pushing the intrinsic  $^{12}\text{C}/^{13}\text{C}$  toward lower or higher values. A dedicated code is required for a full treatment of photodissociation rates and number densities as influenced by a given UV radiation field and chemical abundances (e.g., van Dishoeck & Black 1988; Warin et al. 1996). Instead, we compare our determinations to values and results from van Dishoeck & Black (1988) using a more simplified approach. In analyzing  $^{12}\text{CO}/^{13}\text{CO}$  toward  $\zeta$  Oph, Lambert et al. (1994) introduced a formula that allows an evaluation of the isotopic ratio in terms of the competition between SPD and ICE, namely,

$$F_{13} = \frac{\Gamma_{13} + n(^{12}\text{C}^+)k_1^r}{\Gamma_{12} + n(^{12}\text{C}^+)k_1^f},$$

where  $\Gamma_i$  stands for the photodissociation rate of the isotopologue  $^i\text{CO}$ ,  $k_1^f$  is the forward rate coefficient for the ICE reaction with  $\text{C}^+$ , the number density of which is designated by  $n$ . Without ICE,  $F_{13}$  is simply the ratio of  $\Gamma_{13}$  to  $\Gamma_{12}$ , which for  $N(^{12}\text{CO}) = 10^{14} \text{ cm}^{-2}$  is only 1.2, but is  $\approx 4.5$  for  $N(^{12}\text{CO}) = 10^{16} \text{ cm}^{-2}$  (van Dishoeck & Black 1988, their Table 5). When ICE is the only process operating, the equilibrium value for  $F_{13}$  is  $k_1^r/k_1^f = \exp(-35/T_{\text{kin}})$ , i.e., it depends only on the kinetic temperature of the gas. It will be seen in § 4.8 that the average  $T_{\text{kin}} \approx 60 \text{ K}$ , which leads to  $F_{13} \approx 0.56$ , or a 12-to-13 CO ratio of  $\approx 39$ , under the operation of ICE without SPD. Such a ratio is remarkably similar to the lowest values found in the current survey.

The formula for the photodissociation rate,

$$\Gamma_i = 2.04 \times 10^{-10} I_{\text{UV}} \Theta_i \theta_c \text{ s}^{-1},$$

includes the enhancement in the strength of the UV radiation field,  $I_{\text{UV}}$ , the shielding function of the isotopologue  $^i\text{CO}$ ,  $\Theta_i$ , and the continuum extinction owing to dust,  $\theta_c$  (van Dishoeck & Black 1988). The values for  $\Theta_i$  are extracted via interpolation from Table 5 of van Dishoeck & Black (1988), using one-half of the measured values for  $N(\text{H}_2)$  and  $N(\text{CO})$  as input, as appropriate for a finite modeled slab with equal UV illumination on both sides. Other cloud geometries and/or fragmentation have been shown to significantly affect the CO abundance relative to H and  $\text{H}_2$ , but not to affect the 12-to-13 CO isotopic ratio (Kopp et al. 2000). The continuum dust extinction is parametrized by  $\exp(-\tau_{\text{UV}})$  for the sake of consistency with the chemical modeling (§ 4.5). The number density of ionized carbon,  $n(^{12}\text{C}^+)$ , is computed from  $1.4 \times 10^{-4} n(\text{H})$ , the observed abundance of  $\text{C}^+$  in the ISM (Cardelli et al. 1996). The total gas (hydrogen) number density,  $n_{\text{tot}}(\text{H})$ , is given by  $n_{\text{CN}}$ , which in turn is also determined from chemical modeling of  $N(\text{CN})$  and  $N(\text{CH})$  in § 4.5. The values of  $T_{\text{kin}}$ ,  $I_{\text{UV}}$ ,  $\tau_{\text{UV}}$ ,  $n_{\text{CN}}$ ,  $\Theta_{12}$ , and  $\Theta_{13}$  are given for each sight line in Table 6.

Figure 8 shows observed  $F_{13}$  values (empty squares) versus  $\log N(^{12}\text{CO})$ . Using all the fractionation parameters listed in Table 6, we computed  $\Gamma_{12}$  and  $\Gamma_{13}$ , and then  $F_{13}$  values for all sight lines, which are denoted by the ‘X’ symbols in Fig. 8. The best correspondence between the observed and predicted values was found by minimizing the rms differences between the two sets of  $F_{13}$  values for all sight lines. Such rms minimization was done in order to determine the value of any parameter that best reproduces observed  $F_{13}$  values. When both fractionation processes are operating the predicted  $F_{13}$  values cannot easily reach above  $\approx 1.0$ , unless values that are  $\approx 5$  times higher than those found by the chemical models are incorporated into  $I_{\text{UV}}$ , or values that are  $\approx 5$  times lower are incorporated into  $n(\text{C}^+)$  and/or  $k_1^f$ . Two values have been given in the literature for  $k_1^f$ :  $2 \times 10^{-10} \text{ cm}^3 \text{ s}^{-1}$  (Watson et al. 1976) and  $7.5 \times 10^{-10} \text{ cm}^3 \text{ s}^{-1}$  (Smith & Adams 1980). The smaller value for  $k_1^f$  returns predicted  $^{12}\text{CO}/^{13}\text{CO}$  values that are in better agreement with the observed distribution.

With the Watson et al. (1976) value for  $k_1^f$ , and keeping all other parameters unchanged from their chemical modeling results, one is left with a single ingredient that controls the predicted values of  $F_{13}$ : the shielding function of CO. (More accurately, two such ingredients,  $\Theta_{12}$  and  $\Theta_{13}$ .) Differences between observed  $F_{13}$  values and their predictions are best minimized when both  $\Theta_{12}$  and  $\Theta_{13}$  are increased by a factor of 2. It has been suggested that the shielding functions of CO stand in need for upward revision owing to inconsistencies between isotopic ratio predictions and observations (Sheffer et al. 2002b; Federman et al. 2003). A major contribution to this revision can be provided by an upward revision in the  $f$ -values of Rydberg bands of CO, which should enhance both the SPD of CO under low- $N$  conditions, as well as its self shielding under high- $N$  conditions. Since the latest determinations of Rydberg  $f$ -values for all CO isotopologues demonstrate an upward revision by a factor of  $\approx 2$  (Federman et al. 2001; Sheffer, Federman, Pan, & Andersson 2003; Eidelsberg et al. 2004), incorporating these revised  $f$ -values would presumably help to raise the CO shielding functions by the same factor.

#### 4.5. $^{12}\text{CO}/^{13}\text{CO}$ versus Gas Density

Table 6 provides values for the gas density,  $n_{\text{CN}}$ , that were derived from our chemical modeling of  $N(\text{CH})$  and  $N(\text{CN})$  along these sight lines. A chemical network of formation and destruction processes for CN is evaluated for an assumed

value of  $I_{\text{UV}}$ , subject to dust attenuation by the factor  $\exp(-\tau_{\text{UV}})$ , which is evaluated at 1000 Å. In this modeling,  $\tau_{\text{UV}}$  has the value  $2 \times 3.1 \times E_{B-V}$ , unless extinction curves and the value of  $R_V$  (or  $A_V/E_{B-V}$ ) for a specific direction indicate  $\sim 50\%$  change in the prefactor. This prefactor is about half the value found from extinction curves in order to account for forward scattering by the dust at far UV wavelengths (Federman et al. 1994). The derived values for  $n_{\text{CN}}$  are found to be proportional to the value of  $I_{\text{UV}}$ , but they are found to be very insensitive to the input values of  $T_{\text{kin}}$  of the gas (a detailed description of the analysis will be given in a future paper). Although approximate  $T_{\text{kin}}$  values were used as input (see Table 6),  $n_{\text{CN}}$  should change very little by incorporating  $T_{1,0}(\text{H}_2)$  from Table 7 instead.

Figure 9 displays the behavior of  $^{12}\text{CO}/^{13}\text{CO}$  with respect to  $n_{\text{CN}}$ . The isotopic ratio of CO may show a hint of a mild anti-correlation with  $n_{\text{CN}}$ . However, inspecting other sight line attributes such as  $N$  and  $T_{\text{kin}}$ , we find no obvious association of values of high gas density with higher CO column densities (of either isotopologue), nor with lower kinetic temperature of the gas. Gas density based on the chemical analysis is expected to be applicable to the CO molecule because CO and CN are inferred to coexist spatially in diffuse molecular clouds (Pan et al. 2005). Another derivation of  $I_{\text{UV}}$  and  $n$  from an analysis of high- $J$  levels of  $\text{H}_2$  returns extremely inflated values, as described in § 4.10.

#### 4.6. $^{12}\text{CO}/^{13}\text{CO}$ versus $^{12}\text{CN}/^{13}\text{CN}$

Other carbon-bearing molecules such as CN also show appreciable variations in fractionation when probed via (optical) absorption. As opposed to CO, the CN molecule is dissociated by continuum radiation (Lavendy et al. 1987) and is not expected to show fractionation to higher values caused by isotopic-selective photodissociation. On the other hand, the zero-energy difference of 31 K (Bakker & Lambert 1998) that favors the heavier  $^{13}\text{CN}$  isotopologue, will work to fractionate CN toward lower 12-to-13 ratios, especially at low temperatures. However, when the more abundant CO molecule incorporates most of the  $^{13}\text{C}$  atoms from the ambient gas, the 12-to-13 ratio of other molecular species, such as CN and  $\text{H}_2\text{CO}$  increases, producing fractionation opposite to that of CO. Two sight lines offer evidence for this effect happening in CN: toward  $\zeta$  Oph, Roth & Meyer (1995) measured  $^{12}\text{CN}/^{13}\text{CN} = 35 \pm 11$ , whereas Lambert et al. (1994) determined  $^{12}\text{CO}/^{13}\text{CO} = 167 \pm 25$ ; as well as toward HD 154368, where Palazzi et al. (1990) found the CN 12-to-13 ratio to be  $101 \pm 12$ , and this paper shows that the CO 12-to-13 ratio is  $37 \pm 8$ . Thus these two sight lines show CN to have an opposite sense of fractionation to that of CO, a situation that arises when the more abundant CO controls the availability of  $^{13}\text{C}$  atoms. As a result of their anti-correlation both CO and CN 12-to-13 values from UV determinations are seen to vary within a factor-of-2 range about the reference value of  $^{12}\text{C}/^{13}\text{C} = 70$ . Simultaneously,  $^{12}\text{CH}^+ / ^{13}\text{CH}^+$  values are not fractionated:  $68 \pm 5$  toward  $\zeta$  Oph (Crane et al. 1991) and  $58 \pm 8$  toward HD 154368 (Casassus et al. 2005). Thus the CN and CO isotopic ratios along each sight line are found on opposite sides of the  $\text{CH}^+$  (and the ambient carbon) isotopic ratio. Another sight line suggests a high value of  $^{12}\text{CN}/^{13}\text{CN}$ , namely  $122 \pm 33$  toward HD 21483 (Meyer et al. 1989), but no information is available concerning the  $^{12}\text{CO}/^{13}\text{CO}$  in that direction. Finally, toward  $\zeta$  Per,  $^{12}\text{CO}/^{13}\text{CO}$  of  $108 \pm 5$  shows it to be moderately fractionated, whereas  $^{12}\text{CN}/^{13}\text{CN} = 77^{+27}_{-18}$  was given in Kaiser et al. (1991). Given the smaller level of CO fractionation and the relatively large uncertainties in the CN isotopic ratio, any final determination will have to be based on data with better S/N. Interestingly, establishing a relationship of opposite fractionation between CO and CN is tantamount to showing that both molecules coexist spatially in the ISM, allowing them to interact with the same pool of  $^{13}\text{C}$  atoms.

#### 4.7. Excitation Temperature of $^{12}\text{CO}$ and $^{13}\text{CO}$

Each spectrum synthesis with Ismod.f returned fitted values for the excitation temperature  $T_{\text{ex}} = T_{J'',0}$  based on the relative populations in the ground state ( $J'' = 0$ ) and in any higher- $J''$  excited level. The average values of  $T_{1,0}$  for both isotopologues agree with each other very well:  $T_{\text{ex}}(^{12}\text{CO}) = 3.7 \pm 0.9$  K, and  $T_{\text{ex}}(^{13}\text{CO}) = 3.9 \pm 1.2$  K. The analysis above in § 2 showed that both isotopologues agree very well in radial velocity, providing kinematic support for their spatial coexistence. Having indistinguishable  $T_{\text{ex}}$  values provides additional strong support that both CO isotopologues are well mixed and are subject to the same physical conditions. The smaller samples of Burgh et al. (2007) and Sonnentrucker et al. (2007) also indicated the same  $T_{\text{ex}}$  for the two CO isotopologues within the stated uncertainties. The mm-wave absorption survey of CO (Liszt & Lucas 1998) tabulated  $T_{\text{ex}}$  values that provide the averages  $6.2 \pm 1.2$  and  $5.6 \pm 0.7$  K for  $^{12}\text{CO}$  and  $^{13}\text{CO}$ , respectively, also showing them to be identical within the uncertainties. These mm-wave-derived  $T_{\text{ex}}$  values are higher than the UV-derived values, suggesting that denser gas is being observed and that the two samples may be different.

#### 4.8. Lower $T_{1,0}(\text{H}_2)$ along Sight Lines with $^{13}\text{CO}$

The kinetic temperature of the gas is well approximated by  $T_{1,0}(\text{H}_2)$ , because  $\text{H}_2$  is a homonuclear molecule, so that the relative level populations of the ortho and para ground states are controlled by collisions characterized by  $T_{\text{kin}}$ . From the 22 sight lines with  $\text{H}_2$  data in our  $^{13}\text{CO}$  sample, the average  $T_{1,0}(\text{H}_2) = 60 \pm 8$  K. This value is lower by 17 and 8 K, respectively, than  $T_{1,0}$  averages of  $77 \pm 17$  K found by Savage et al. (1977), and  $68 \pm 15$  K from Rachford et al. (2002), both of which were  $\text{H}_2$  surveys unrelated to the presence of CO. It appears that  $\text{H}_2$  (and thus, the gas in general) is colder along sight lines with detectable amounts of  $^{13}\text{CO}$ . Since all targets in this paper were selected *a priori* to show measurable amounts of  $^{13}\text{CO}$  in their spectra, this selection criterion and the presence of lower kinetic gas temperatures seem to be related. In order to verify that  $T_{1,0}$  is lower when  $^{13}\text{CO}$  is present, we must analyze sight lines from surveys dedicated to CO.

Sonnentrucker et al. (2007) presented a literature compilation with 38  $T_{1,0}(\text{H}_2)$  values from CO-bearing sight lines, yielding an average  $T_{1,0}$  of  $69 \pm 16$  K. However, splitting the sample into sight lines with or without detected amounts of  $^{13}\text{CO}$ , we find that  $T_{1,0} = 56 \pm 8$  K from 12 directions with  $^{13}\text{CO}$ , whereas  $T_{1,0} = 76 \pm 15$  K from 26 sight lines without detected  $^{13}\text{CO}$ , or  $\Delta T_{1,0} = 20$  K. Burgh et al. (2007) found an average  $T_{1,0}$  of  $74 \pm 24$  K for 23 CO sight lines. When we split their sample according to  $^{13}\text{CO}$  detectability, six  $^{13}\text{CO}$  directions have  $T_{1,0} = 58 \pm 8$  K, while 17 without  $^{13}\text{CO}$  have  $T_{1,0} = 80 \pm 25$  K, or  $\Delta T_{1,0} = 22$  K. This shows that sight lines with  $^{13}\text{CO}$  from both CO samples have average  $T_{1,0}$  values that are in extremely good agreement with our average of  $60 \pm 8$  K. Furthermore, the selection of sight lines with detectable amounts of  $^{13}\text{CO}$  appears to sample  $\text{H}_2$  molecules that are colder by  $\approx 20$  K, or equivalently, regions of ambient gas with  $T_{\text{kin}}$  that is  $\approx 20$  K lower than along other directions.

In fact, this clear separation of sight lines into two groups according to their  $^{13}\text{CO}$  abundance can provide an explanation for the lower *FUSE* average for  $T_{1,0}$  found by Rachford et al. (2002) relative to the *Copernicus* value from Savage et al. (1977). Ten of the 23 sight lines in the Rachford et al. (2002) sample have detectable amounts of  $^{13}\text{CO}$ ; thus 43% of that sample is expected to show the presence of colder gas. The 13 sight lines without  $^{13}\text{CO}$  provide  $T_{1,0} = 73 \pm 16$  K, whereas the ones with  $^{13}\text{CO}$  have  $T_{1,0} = 60 \pm 9$  K, i.e., a difference of 13 K. One can observe that the colder value of  $T_{1,0}$  is in excellent agreement with the average  $T_{1,0}$  of our  $^{13}\text{CO}$  sight lines, while the warmer value of  $T_{1,0}$  agrees nicely with the average  $T_{1,0}$  from Savage et al. (1977), which by inspection had 55 lines without detections of  $^{13}\text{CO}$ , averaging  $T_{1,0} = 79 \pm 15$  K. This *Copernicus* sample included only six sight lines currently known to have  $^{13}\text{CO}$  that, unsurprisingly, yield the low  $T_{1,0} = 52 \pm 7$  K, or 27 K below the value for clouds without  $^{13}\text{CO}$ . Since the Rachford et al. (2002) sample was designed to explore translucent sight lines with higher  $A_V$  and higher  $N(\text{H}_2)$ , such physical and chemical conditions seem to promote the formation and survival of detectable amounts of  $^{13}\text{CO}$ . In fact, the current sample has very similar characteristics to that of Rachford et al. (2002): average value of  $A_V$  is  $1.4 \pm 0.5$  versus  $1.6 \pm 0.7$ , and average value of  $\log N(\text{H}_2) = 20.7 \pm 0.2$  versus  $20.8 \pm 0.2$ . It is also interesting that Rachford et al. (2002) remarked that nine *Copernicus* sight lines with  $\log N(\text{H}_2) = 20.7$  averaged to  $55 \pm 8$  K, reinforcing the interconnectedness between higher  $\text{H}_2$  column density, lower gas kinetic temperature, and the presence of diatomic molecules with heavy elements such as  $^{13}\text{CO}$  (see below). The inverse correspondence between the presence of  $^{13}\text{CO}$  and  $T_{1,0}$  may be used to predict detectable abundances of  $^{13}\text{CO}$  along sight lines that have  $T_{1,0}(\text{H}_2) \lesssim 65$  K.

A few of the directions with  $^{13}\text{CO}$  analyzed in this paper were selected from a larger sample of CO sight lines for which we also determined  $T_{1,0}(\text{H}_2)$ , based on cloud structures from newly acquired high- $R$  *McD* and *ESO* optical spectra. For the sake of consistency, the average  $T_{\text{kin}}$  for the gas along all other sight lines should also be established. Yet again, 30 directions without  $^{13}\text{CO}$  return  $T_{1,0} = 79 \pm 13$  K, whereas the four with  $^{13}\text{CO}$  yield  $T_{1,0} = 59 \pm 10$  K, showing what by now seems to be the “canonical”  $\Delta T_{1,0}$  of  $\approx 20$  K between the two groups of sight lines as sorted by the presence of  $^{13}\text{CO}$ .

#### 4.9. $^{13}\text{CO}$ and Other Heavy Diatomic C-bearing Molecules

We also inspected the literature survey in Sonnentrucker et al. (2007) according to the presence or absence of carbon-bearing diatomic molecules other than CO and found that  $^{13}\text{CO}$  is not the only molecule revealing two groupings of cooler or warmer  $\text{H}_2$  gas. Nine sight lines without detected amounts of  $\text{C}_2$  yielded  $T_{1,0}(\text{H}_2) = 83 \pm 16$  K, whereas 17 directions with  $\text{C}_2$  returned the average  $57 \pm 9$  K, or  $\Delta T_{1,0} = 26$  K. The agreement of  $T_{1,0}$  from  $\text{C}_2$  sight lines with the  $^{13}\text{CO}$  sight lines in § 4.8 is outstanding. As for CN, 10 sight lines without detectable amounts of this molecule average to  $T_{1,0}(\text{H}_2) = 79 \pm 13$  K, while 28 directions with detections provide  $66 \pm 16$  K, or  $\Delta T_{1,0} = 13$  K. These results further enhance the correspondences found between CO, CN, and  $\text{C}_2$  (e.g., Federman et al. 1994; Pan et al. 2005; Sonnentrucker et al. 2007).

The most straightforward connection between  $T_{\text{kin}}$  of the gas and the abundance of  $^{13}\text{CO}$  is provided by the exponential dependence of the ICE reaction. In colder gas the ICE reaction is faster and more efficient in converting  $^{13}\text{C}^+$  to  $^{13}\text{CO}$ . Nevertheless, lowering  $T_{\text{kin}}$  from 80 K along directions without  $^{13}\text{CO}$  to 60 K along those with  $^{13}\text{CO}$  brings about a decrease of only 15% in  $^{12}\text{CO}/^{13}\text{CO}$ . However, owing to a much more extended sight-line distribution of  $\text{H}_2$  in comparison with CO,  $T_{1,0}(\text{H}_2)$  may not provide the best indication of  $T_{\text{kin}}$  for  $^{13}\text{CO}$ . The more concentrated distribution of heavier molecules has been shown to exist for CN and CO (Pan et al. 2005), as well as for  $\text{C}_2$  (Federman et al. 1994; Sonnentrucker et al. 2007). These three molecules contain two heavy elements and are found in denser and colder clumps of gas with  $T_{\text{kin}}$  that is better estimated from  $T_{\text{ex}} = T_{2,0}$  of rotational populations in  $\text{C}_2$ . Sonnentrucker et al. (2007) tabulated  $T_{2,0}$  values for  $\text{C}_2$  and mentioned that they are lower than  $T_{1,0}(\text{H}_2)$ . Their Table 14 reveals that nine sight lines common to  $\text{H}_2$  and  $\text{C}_2$  have average  $T_{1,0}(\text{H}_2)$  of  $58 \pm 9$  K, whereas the average of  $T_{2,0}(\text{C}_2)$  is  $28 \pm 11$  K, showing that  $\text{C}_2$  is colder by 30 K. If the latter is taken to measure  $T_{\text{kin}}$  of the gas inside the denser and colder molecular clumps that also include  $^{13}\text{CO}$ , then one finds a 50 K drop between environments with and without  $^{13}\text{CO}$ . This translates into a factor of  $\sim 2$  higher efficiency for the ICE conversion of  $^{13}\text{C}^+$  into  $^{13}\text{CO}$ , which can nicely account for the those VUV sight lines with CO that is observed to be fractionated by the same factor.

#### 4.10. Is $^{12}\text{CO}/^{13}\text{CO}$ Related to High Excitation Levels of $\text{H}_2$ ?

The following assumes that the population of higher rotational levels of  $\text{H}_2$  can be described by a steady state relation between the formation of rotationally-excited  $\text{H}_2$  molecules and UV pumping from the ground state on one hand, and level depopulation by spontaneous radiative emission on the other. Lee et al. (2002) provide a couple of equations that



compute the gas density,  $n_{\text{tot}}(\text{H})$ , and the radiation field enhancement,  $I_{\text{UV}}$ , from the observed populations of the  $J'' = 0, 1$ , and 4 levels of  $\text{H}_2$ . These equations are based on the simplified model of Jura (1974, 1975), which included a set of assumptions, such as the lack of dust absorption in  $\text{H}_2$  Lyman bands ( $\sim 1000 \text{ \AA}$ ) and  $n_{\text{tot}}(\text{H}) < 10^4 \text{ cm}^{-3}$ , which allows spontaneous emission to proceed without significant competition from collisional de-excitation. Table 7 provides hydrogen-related parameters, including Ismod.f modeling values for  $N_{\text{tot}}(\text{H}_2)$ ,  $T_{1,0}$ , and  $T_{4,0}$  (the complete set of results will appear elsewhere). Although we synthesized the available  $\text{H}_2$  level populations for 16 sight lines, only 10 of them were found to have published  $N(\text{H})$  values, which are needed for  $N_{\text{tot}}(\text{H})$ . The references for  $N(\text{H})$  were six sight lines from Diplas & Savage (1994), three sight lines from Cartledge et al. (2004), and a single sight line from Lacour et al. (2005). Also given in Table 7 are values for  $I_{\text{UV}}$  and  $n_{\text{tot}}(\text{H})$  that were derived using the equations in Lee et al. (2002).

When  $^{12}\text{CO}/^{13}\text{CO}$  is plotted versus the  $\text{H}_2$ -derived  $I_{\text{UV}}$  or versus  $n_{\text{tot}}(\text{H})$ , there seems to be no discernible correlation. In fact, since both  $n_{\text{tot}}(\text{H})$  and  $I_{\text{UV}}$  have much higher derived values than those determined in the modeling based on CN chemistry (Table 6), the conclusion is that CO is not associated with regions containing rotationally excited  $\text{H}_2$ . This confirms that CO is concentrated in denser and colder regions that are much less extended than the distribution of  $\text{H}_2$ , but are closely related to the conditions inferred from analysis of CN absorption (§ 4.5). It is notable that some  $\text{H}_2$ -derived  $n_{\text{tot}}(\text{H})$  values exceed the underlying model assumption (Jura 1974, 1975) that it be  $< 10^4 \text{ cm}^{-3}$ , showing that the equations are not adequate for the analysis of some of these sight lines. Furthermore, the chemical model explicitly includes dust extinction at  $1000 \text{ \AA}$ .

A more proper gauge of the enhancement in UV excitation is provided by analyzing vibrationally-excited absorption lines from  $\text{H}_2$  (Federman et al. 1995). The three sight lines with significant upward CO fractionation are the ones published before by Federman et al. (1995) and Federman et al. (2003), two of which exhibited detectable vibrationally-excited  $\text{H}_2$ :  $\zeta$  Oph and  $\rho$  Oph A. The predominance of selective photodissociation in the fractionation of CO is thus confirmed by the presence of vibrationally-excited lines of  $\text{H}_2$ , since searching for the same lines failed to detect them in other sight lines with unfractionated or downward-fractionated CO, even those with the highest values of  $N(\text{CO})$ .

## 5. COMPARISON WITH $^{12}\text{CO}/^{13}\text{CO}$ FROM OTHER SPECTRAL REGIMES

As mentioned in § 4.1, the bottom panel in Fig. 6 shows a histogram of the VUV 12-to-13 results. Proceeding topward, other histograms show 12-to-13 ratios from optical observations of  $\text{CH}^+$ , mm-wave absorption observations of CO, mm-wave absorption results from the non-CO molecules  $\text{HCO}^+$ , HCN, and HNC, and lastly the three mm-wave emission proxies CN, CO, and  $\text{H}_2\text{CO}$ . There seems to be good agreement between sample averages (centering) and the carbon isotopic ratio of 70 (dashed line) from Wilson (1999), which was based on the top two samples. The mm-wave absorption survey of CO by Liszt & Lucas (1998) is responsible for the only histogram with a different distribution.

Some support for UV-derived CO isotopic ratios that are fractionated upward comes from the NIR observations of Goto et al. (2003), who measured  $^{12}\text{CO}/^{13}\text{CO}$  of  $137 \pm 9$  toward LkH $\alpha$  101 and 158 (uncertainty unknown) toward Mon R2 IRS 3, i.e., fractionated upward by a factor of  $\sim 2$ . These targets are heavily reddened molecular clouds, illuminated by background IR sources deeply embedded in star-forming regions, with  $N(^{12}\text{CO}) = 2 \times 10^{18}$  to  $2 \times 10^{19} \text{ cm}^{-2}$ , or 100 to 1000 times greater than the largest values ( $\sim 10^{16} \text{ cm}^{-2}$ ) here. As stated by Goto et al. (2003), one would not expect high isotopic values under conditions of very high extinction that prevent the operation of SPD. Goto et al. (2003) note that their fitted  $T_{\text{ex}}$  values for the cool components of  $^{12}\text{CO}$  (seen in the transitions with  $J \lesssim 6$ ) are about twice as high as  $T_{\text{ex}}$  values of  $^{13}\text{CO}$ , owing to photon trapping in  $^{12}\text{CO}$  transitions. Since the inferred  $N$  values are proportional to  $T_{\text{ex}}$ , the results show isotopic ratios about twice as high as the ambient value of 70.

Studies of mm-wave *absorption* toward extragalactic sources have yielded molecular isotopic ratios appreciably lower than the ambient  $^{12}\text{C}/^{13}\text{C}$ . Lucas & Liszt (1998) found  $59 \pm 2$  to be the weighted average of 12-to-13 obtained from absorption profiles of three non-CO carbon-bearing species:  $\text{HCO}^+$ , HCN, and HNC. The derived average included six absorption components mostly toward a single galactic direction, whereas one component that yielded  $\text{H}^{12}\text{CN}/\text{H}^{13}\text{CN} = 170 \pm 51$  was too anomalous to be included in the average. Lucas & Liszt (1998) analyzed five sight lines and found  $N(^{12}\text{CO})/N(^{13}\text{CO})$  to range from  $15.3 \pm 2.1$  to  $54 \pm 13$ . Four sight lines from this highly-fractionated sample show at a significance better than  $4 \sigma$  that  $^{13}\text{CO}$  is enhanced by up to a factor of 4.6, which compares favorably with predicted model values for very cold clouds (van Dishoeck & Black 1988). However, as noted by Liszt & Lucas (1998), such mm-wave observations are difficult to interpret owing to long path lengths and complicated cloud structures. Their lowest 12-to-13 CO ratios (down to 15) refer to the sight line toward B0355+508, which presents five kinematic components along a very long path through the molecular layer of the Galactic disk. We estimate the upper limit on the path length to be 8.7 kpc from  $243 \text{ pc}/\sin(11^\circ)$  based on the  $3 \sigma$  scale height of the molecular component of the ISM (Cox 2005). Since this sight line is  $150^\circ$  away from the direction to the Galactic center, resulting in an upper limit of 16.6 kpc for  $D_{\text{GC}}$ , its very low  $^{12}\text{CO}/^{13}\text{CO}$  values stand in stark contrast to the Galactic gradient of 12-to-13 being proportional to  $D_{\text{GC}}$  (Wilson & Rood 1994; Wilson 1999; Savage et al. 2002; Milam et al. 2005). We surmise that very cold gas is being probed so that the ICE reaction is even more effective in producing  $^{13}\text{CO}$  than in more local and warmer gas. This would be consistent with the findings of Lequeux et al. (1993) for molecular gas in the outer Galaxy.

Bensch et al. (2001), while reporting the first mm-wave detection of  $^{13}\text{C}^{17}\text{O}$  emission in the ISM, also reported  $\text{C}^{17}\text{O}/^{13}\text{C}^{17}\text{O}$  of  $65 \pm 11$  toward the molecular cloud core  $\rho$  Oph C, using beam sizes of  $25''$  to  $50''$ . This unfractionated value sharply contrasts with the Federman et al. (2003) VUV value of  $^{12}\text{CO}/^{13}\text{CO} = 125 \pm 23$  in absorption toward

the star  $\rho$  Oph A. A way to reconcile this difference in results from the two spectral regimes is to attribute it to the different volumes being probed by the observing techniques. The VUV isotopic ratio probes the outer parts of the cloud that absorb the stellar and interstellar radiation, sampling  $N(^{12}\text{CO})$  of  $\sim 2 \times 10^{15} \text{ cm}^{-2}$  that is sufficient for self shielding by  $^{12}\text{CO}$ , but leaves  $^{13}\text{CO}$  molecules subjected to high UV flux levels that drive  $F_{13}$  up to 1.8. On the other hand, the mm-wave  $\text{C}^{17}\text{O}$ -to- $^{13}\text{C}^{17}\text{O}$  ratio tells us that deeper inside the cloud, where  $N(^{12}\text{CO})$ ,  $N(^{13}\text{CO})$ , and  $N(\text{C}^{18}\text{O})$  are  $\approx 10^{19}$ ,  $10^{17}$ , and  $10^{16} \text{ cm}^{-2}$ , respectively, there is no UV flux and, thus, no CO fractionation. Since the volume explored by UV absorption lines has a column density  $\sim 10^4$  smaller than that of the volume explored by mm-wave emission, the star  $\rho$  Oph A is either situated in front of the bulk of the CO, or is shining through the outer envelope of the molecular cloud core.

## 6. CONCLUDING REMARKS

We surveyed the *HST* archive to assemble a sample of 25 diffuse and translucent (i.e.,  $0.65 \leq A_V \leq 2.58$ ) sight lines with absorption signatures from  $^{13}\text{CO}$ . Most of these sight lines are consistent with no fractionation of CO away from the ambient  $^{12}\text{C}/^{13}\text{C} = 70$ , while 32% are found to be significantly fractionated. Two photochemical processes compete in driving  $^{12}\text{CO}/^{13}\text{CO}$  away from 70: SPD in diffuse clouds destroys less of  $^{12}\text{CO}$  thanks to self shielding, whereas the ICE reaction enhances the abundance of  $^{13}\text{CO}$  in colder clouds. The former cases are confirmed by the presence of  $\text{H}_2$  absorption lines that are vibrationally excited by the enhanced UV radiation field.

Three regimes of  $^{12}\text{CO}$  column density were seen to correspond to varying contributions from SPD and ICE in affecting CO fractionation. In the lowest- $N(^{12}\text{CO})$  regime, 12-to-13 values are  $\geq 70$  owing to self shielding by  $^{12}\text{CO}$  and insignificant competition from ICE. In the middle regime, where  $^{12}\text{CO}/^{13}\text{CO}$  revealed the lowest values in the UV, as well as an overlap with mm-wave absorption results, the presence of  $\text{C}^+$  allows the ICE reaction to produce efficiently higher amounts of  $^{13}\text{CO}$ . Finally, the highest- $N(^{12}\text{CO})$  regime presents the deepest part of the clouds, where shielding applies to both isotopologues, resulting in  $^{12}\text{CO}/^{13}\text{CO}$  values close to 70.

The simple model of the fractionation, based on the Lambert et al. (1994) formula for  $F_{13}$ , allowed us to evaluate the basic ingredients that affect fractionation, leading to a preference of the Watson et al. (1976) value for the forward reaction between  $^{13}\text{C}^+$  and  $^{12}\text{CO}$  over that published by Smith & Adams (1980) and indicating the need to increase CO self shielding functions by  $\sim 2$ . However, this simplified model should be followed by more detailed computations that will include the newly available set of larger (also by  $\sim 2$ )  $f$ -values of CO.

It now appears that the detection of  $^{13}\text{CO}$  can be statistically associated with the presence of cold gas. The analysis of  $T_{1,0}(\text{H}_2)$  showed that  $\text{H}_2$  is cooler by about 20 K along sight lines that possess detectable amounts of  $^{13}\text{CO}$ . Furthermore, two other carbon-bearing molecules agree with this scenario, since both CN and  $\text{C}_2$  are also associated with  $\text{H}_2$  that is colder. When ICE is the sole fractionating process,  $T_{\text{kin}}$  of 60 K will establish an equilibrium value of  $^{12}\text{CO}/^{13}\text{CO} \approx 40$ , which agrees very well with the lowest isotopic values in the present VUV sample. However, no clear correlation is seen between the 12-to-13 ratio and  $T_{\text{kin}}$ , presumably because it is masked by the competing route to fractionation, namely SPD, that affects each sight line to a different extent.

Besides narrow  $b$ -values that are common to CO and CN absorption lines, the opposite fractionation relationship that was found between  $^{12}\text{CO}/^{13}\text{CO}$  and  $^{12}\text{CN}/^{13}\text{CN}$  also supports the coexistence of CN and CO. Together with  $\text{C}_2$ , all three molecules are associated with colder  $\text{H}_2$  gas. The inferred coexistence of CO, CN, and  $\text{C}_2$  in denser and colder portions of a cloud promotes  $T_{2,0}(\text{C}_2)$  instead of  $T_{1,0}(\text{H}_2)$  as the better probe of  $T_{\text{kin}}$  of the gas in which  $^{13}\text{CO}$  is found. When  $T_{\text{kin}} \approx 30$  K is assumed, the ICE reaction for CO fractionation will achieve an equilibrium value of  $\approx 20$  in the absence of SPD. Although we do not see such low values here, similar values have been found for CO in mm-wave absorption studies (Liszt & Lucas 1998). It remains to be seen whether the mm-wave sample is, indeed, free of UV photodissociation effects, and whether the VUV CO isotopic ratios happen to hover above  $\approx 40$  owing to competition from SPD.

Fractionation prevents molecular proxies from perfectly tracking the atomic carbon ratios, thus direct results concerning the distribution of  $^{12}\text{C}$  and  $^{13}\text{C}$  will eventually have to come from observations of atomic forms of carbon. A few steps in this direction were taken by Boreiko & Betz (1996), Keene et al. (1998), and Tieftrunk et al. (2001). Along two lines of sight only a few arcminutes apart and near the Trapezium cluster at the center of the Orion Nebula, Boreiko & Betz (1996) detected  $158 \mu\text{m}$  emission from both  $^{12}\text{C}^+$  and  $^{13}\text{C}^+$ , whereas Keene et al. (1998) observed 809 GHz emission from both  $^{12}\text{C}^0$  and  $^{13}\text{C}^0$ . The two studies yielded the same ratio for  $^{12}\text{C}/^{13}\text{C}$ :  $58 \pm 6$  and  $58 \pm 12$ , respectively. Keene et al. (1998) also measured  $^{12}\text{C}^{18}\text{O}/^{13}\text{C}^{18}\text{O} = 75 \pm 9$ . All three results agree with the solar neighborhood value of 70, considering the quoted uncertainties. Still, even  $^{12}\text{C}/^{13}\text{C}$  may get modified by competition with molecules, especially CO, for the availability of  $^{13}\text{C}$ , so that a fuller account of the carbon budget will have to include all of its isotopes in all atomic and molecular combinations, and in all stages of ionization, to properly deduce the details of the photochemistry involved. On the theoretical front, expanding photodissociation and ICE predictions to molecules other than CO (e.g., CN) would allow a better understanding of isotopic results that are being assembled for various sight lines.

We thank NASA for grant NNG04GD31G and STScI for grant HST-AR-09921.01-A. Data files for this paper were accessed through the Multiwavelength Archive at STScI. M. R. acknowledges support by the National Science Foundation under Grant No. 0353899 for the Research Experience for Undergraduates in the Dept. of Physics and Astronomy at the University of Toledo. We are grateful to E. Jenkins for sharing STIS data, and to D. Welty and K.

Pan for providing us with cloud structures from optical CH spectra.

## REFERENCES

- Anders, E., & Grevesse, N. 1989, *Geochim. Cosmochim. Acta*, 53, 197
- Andersson, B.-G., Wannier, P. G., & Crawford, I. A. 2002, *MNRAS*, 334, 327
- Bakker, E. J., & Lambert, D. L. 1998, *ApJ*, 502, 417
- Bally, J., & Langer, W. D. 1982, *ApJ*, 255, 143
- Balser, D. S., McMullin, J. P., & Wilson, T. L. 2002, *ApJ*, 572, 326
- Bensch, F., Pak, I., Wouterloot, J. G. A., Klapper, G., & Winnewisser, G. 2001, *ApJ*, 562, L185
- Boogert, A. C. A., Blake, G. A., & Tielens, A. G. G. M. 2002, *ApJ*, 577, 271
- Boogert, A. C. A., Ehrenfreund, P., Gerakines, P. A., Tielens, A. G. G. M., Whittet, D. C. B., Schutte, W. A., van Dishoeck, E. F., de Graauw, Th., Decin, L., & Prusti, T. 2000, *A&A*, 353, 349
- Boreiko, R. T., & Betz, A. L. 1996, *ApJ*, 467, L113
- Bowers, C. W. 1998, in 1997 HST Calibration Workshop, ed. S. Casertano et al. (Baltimore: Space Telescope Science Institute), 18
- Burgh, E. B., France, K., & McCandliss, S. R. 2007, *ApJ*, 658, 446
- Cardelli, J. A., Meyer, D. M., Jura, M., & Savage, B. D. 1996, *ApJ*, 467, 334
- Cartledge, S. I. B., Lauroesch, J. T., Meyer, D. M., & Sofia, U. J. 2004, *ApJ*, 613, 1037
- Casassus, S., Stahl, O., & Wilson, T. L. 2005, *A&A*, 441, 181
- Chan, W. F., Cooper, G., & Brion, C. E. 1993, *Chem. Phys.*, 170, 123
- Clegg, R. E. S., Storey, P. J., Walsh, J. R., & Neale, L. 1997, *MNRAS*, 284, 348
- Cox, D. P. 2005, *ARA&A*, 43, 337
- Crane, P., Hegyi, D. J., & Lambert, D. L. 1991, *ApJ*, 378, 181
- Diplas, A., & Savage, B. D. 1994, *ApJS*, 93, 211
- Eidelsberg, M., Jolly, A., Lemaire, J. L., Tchang-Brillet, W.-., Breton, J., & Rostas, F. 1999, *A&A*, 346, 705
- Eidelsberg, M., Lemaire, J. L., Fillion, J. H., Rostas, F., Federman, S. R., & Sheffer, Y. 2004, *A&A*, 424, 355
- Federman S. R. 1986, *ApJ*, 309, 306
- Federman S. R., Strom, C. J., Lambert, D. L., Cardelli, Jason A., Smith, V. V., & Joseph, C. L. 1994, *ApJ*, 424, 772
- Federman S. R., Cardelli, J. A., van Dishoeck, E. F., Lambert, D. L., & Black, J. H. 1995, *ApJ*, 445, 325
- Federman S. R., Fritts, M., Cheng, S., Menningen, K. M., Knauth, D. C., & Fulk, K. 2001, *ApJS*, 134, 133
- Federman S. R., Lambert, D. L., Sheffer, Y., Cardelli, J. A., Andersson, B.-G., van Dishoeck, E. F., & Zsargó, J. 2003, *ApJ*, 591, 986
- Fruscione, A., Hawkins, I., Jelinsky, P., & Wiercigroch, A. 1994, *ApJS*, 94, 127
- Goto, M., Usuda, T., Takato, N., Hayashi, M., Sakamoto, S., Gaessler, W., Hayano, Y., Iye, M., Kamata, Y., Kanzawa, T., & 10 coauthors 2003, *ApJ*, 598, 1038
- Hawkins, I., Craig, N., Meyer, D. M. 1993, *ApJ*, 407, 185
- Hawkins, I., & Jura, M. 1987, *ApJ*, 317, 926
- Hawkins, I., & Meyer, D. M. 1989, *ApJ*, 338, 888
- Henkel, C., Wilson, T. L., & Bieging, J. 1982, *A&A*, 109, 344
- Jenkins, E. B., & Tripp, T. M. 2001, *ApJS*, 137, 297
- Jensen, A. G., Rachford, B. L., & Snow, T. P. 2005, *ApJ*, 619, 891
- Jura, M. 1974, *ApJ*, 191, 375
- Jura, M. 1975, *ApJ*, 197, 581
- Kaczmarczyk, G. 2000, *MNRAS*, 316, 875
- Kahane, C., Cernicharo, J., Gomez-Gonzalez, J., & Guelin, M. 1992, *A&A*, 256, 235
- Kaiser, M. E., Wright, E. L., & Hawkins, I. 1991, *ApJ*, 379, 267
- Keene, J., Schilke, P., Kooi, J., Lis, D. C., Mehringer, D. M., & Phillips, T. G. 1998, *ApJ*, 494, L107
- Kopp, M., Roueff, E., & Pineau des Forêts, G. 2000, *MNRAS*, 315, 37
- Lacour, S., Andr M. K., Sonnentrucker, P., Le Petit, F., Welty, D. E., Desert, J.-M., Ferlet, R., Roueff, E., & York, D. G. 2005, *A&A*, 430, 967
- Lambert, D. L., Gustafsson, B., Eriksson, & K., Hinkle, K. H. 1986, *ApJS*, 62, 373
- Lambert, D. L., Sheffer, Y., Gilliland, R. L., & Federman, S. R. 1994, *ApJ*, 420, 756
- Langer, W. D., & Penzias, A. A. 1990, *ApJ*, 357, 477
- Lavendy, H., Robbe, J. M., & Gandara, G. 1987, *J. Phys. B: At. Mol. Phys.*, 20, 3067
- Le Coupanec, P., Rouan, D., Moutou, C., & Léger, A. 1999, *A&A*, 347, 669
- Lee, D.-H., Min, K.-W., Federman, S. R., Ryu, K.-S., Han, W.-Y., Nam, U.-W., Chung, H.-S., Dixon, W. V. D., & Hurwitz, M. 2002, *ApJ*, 575, 234
- Lequeux, J., Allen, R. J., & Guilloteau, S. 1993, *A&A*, 280, L23
- Lucas, R., & Liszt, H. S. 1998, *A&A*, 337, 246
- Liszt, H. S., & Lucas, R. 1998, *A&A*, 339, 561
- Meyer, D. M., Roth, K. C., & Hawkins, I. 1989, *ApJ*, 343, L1
- Milam, S. N., Savage, C., Brewster, M. A., Ziurys, L. M., & Wyckoff, S. 2005, *ApJ*, 634, 1126
- Morton D. C., & Noreau L. 1994, *ApJS*, 95, 301
- Palazzi, E., Mandolesi, N., Crane, P., Kutner, M. L., Blades, J. C., & Hegyi, D. J. 1990, *ApJ*, 357, 14
- Palla, F., Bachiller, R., Stranghellini, L., Tosi, M., & Galli, D. 2000, *A&A*, 355, 69
- Palla, F., Galli, D., Marconi, A., Stanghellini, L., & Tosi, M. 2002, *ApJ*, 568, L57
- Pan, K., Federman, S. R., Sheffer, Y., & Andersson, B.-G. 2005, *ApJ*, 633, 986
- Rachford, B. L., Snow, T. P., Tumlinson, J., Shull, J. M., Blair, W. P., Ferlet, R., Friedman, S. D., Gry, C., Jenkins, E. B., Morton, D. C., & 5 coauthors 2002, *ApJ*, 577, 221
- Rubin, R. H., Ferland, G. J., Chollet, E. E., & Horstmeier, R. 2004, *ApJ*, 605, 784
- Roth, K. C., & Meyer, D. M. 1995, *ApJ*, 441, 129
- Savage, B. D., Bohlin, R. C., Drake, J. F., & Budich, W. 1977, *ApJ*, 216, 291
- Savage, C., Apponi, A. J., Ziurys, L. M., & Wyckoff, S. 2002, *ApJ*, 578, 211
- Sheffer Y., Federman, S. R., Lambert, D. L., & Cardelli, J. A. 1992, *ApJ*, 397, 482
- Sheffer Y., Federman S. R., & Lambert D. L. 2002, *ApJ*, 572, L95
- Sheffer Y., Lambert D. L., & Federman S. R. 2002, *ApJ*, 574, L171
- Sheffer Y., Federman S. R., Pan, K., & Andersson, B.-G. 2003, *ApJ*, 597, L29
- Simonson, S. C. 1968, *ApJ*, 154, 923
- Smith, D., & Adams, N. G. 1980, *ApJ*, 242, 424
- Sonnentrucker, P., Welty, D. E., Thorburn, J. A., & York, D. G. 2007, *ApJS*, in press
- Stahl, O., & Wilson, T. L. 1992, *A&A*, 254, 327
- Tieftrunk, A. R., Jacobs, K., Martin, C. L., Siebertz, O., Stark, A. A., Stutzki, J., Walker, C. K., & Wright, G. A. 2001, *A&A*, 375, L23
- Valencic, L. A., Clayton, G. C., & Gordon K. D. 2004 *ApJ*, 616, 912
- van Dishoeck E. F., & Black J. H. 1988, *ApJ*, 334, 771
- Walborn, N. R. 1972, *AJ*, 77, 312
- Walborn, N. R. 1973, *AJ*, 78, 1067
- Wannier, P., Andersson, B.-G., Penprase, B. E., Federman, S. R. 1999, *ApJ*, 510, 291
- Warin S., Benayoun J. J., & Viala Y. P. 1996, *A&A*, 308, 535
- Watson, W. D., Anicich, V. G., & Huntress, W. T., Jr. 1976, *ApJ*, 205, L165
- Wegner, W. 2003, *Astron. Nachr.*, 324, 219
- Wilson, T. L., & Rood, R. 1994, *ARA&A*, 32, 191
- Wilson, T. L. 1999, *RPPH*, 62, 143

TABLE 1  
STELLAR DATA FOR  $^{12}\text{CO}/^{13}\text{CO}$  SIGHT LINES<sup>a</sup>

Star	Name	Sp.	$V$ (mag)	$l$ (deg)	$b$ (deg)	$v_{LSR}^b$ (km s <sup>-1</sup> )	$E(B-V)$ (mag)	Ref <sup>c</sup>	Distance (pc)	Ref <sup>d</sup>	$D_{GC}$ (kpc)
HD 22951	40 Per	B0.5 V	4.98	158.92	-16.70	-6.1	0.24	1	280	1	8.8
HD 23180	<i>o</i> Per	B1 III	3.86	160.36	-17.74	-6.7	0.30	2	270	2	8.8
HD 23478		B3 IV	6.69	160.76	-17.42	-6.7	0.25	3	240	1	8.7
HD 24398	$\zeta$ Per	B1 Iab	2.88	162.29	-16.69	-7.1	0.32	1	300	1	8.8
HD 24534	X Per	O9.5 pe	6.10	163.08	-17.14	-7.4	0.59	4	920	2	9.4
HD 27778	62 Tau	B3 V	6.33	172.76	-17.39	-10.2	0.37	4	220	1	8.7
HD 96675		B6 IV	7.6	296.62	-14.57	-10.7	0.30	2	160	1	8.4
HD 99872	HR 4425	B3 V	6.11	296.69	-10.62	-10.4	0.36	2	230	1	8.4
HD 147683	V760 Sco	B4 V	7.05	344.86	+10.09	7.2	0.48	5	280	2	8.2
HD 147933	$\rho$ Oph A	B2.5 V	5.02	353.69	+17.69	10.5	0.45	2	110	2	8.4
HD 148184	$\chi$ Oph	B2 Vne	4.42	357.93	+20.68	11.8	0.55	1	150	1	8.4
HD 148937	NSV 7808	O6 f	6.77	336.37	-0.22	3.2	0.67	6	1300	2	7.3
HD 149757	$\zeta$ Oph	O9 V	2.58	6.28	+23.59	14.0	0.32	2	140	1	8.4
HD 154368	V1074 Sco	O9 Ia	6.18	349.97	+3.22	7.9	0.78	4	1400	2	7.1
HD 177989		B2 II	9.34	17.81	-11.88	12.6	0.23	1	5100	2	4.0
HD 192035	RX Cyg	B0 IIIIn	8.22	83.33	+7.76	17.3	0.28	1	2800	2	8.6
HD 198781	HR 7993	B0.5 V	6.46	99.94	+12.61	14.7	0.35	2	640	2	8.6
HD 203374A		B0 IVpe	6.69	100.51	+8.62	14.2	0.60	7	670	2	8.7
HD 203532	HR 8176	B3 IV	6.36	309.46	-31.74	-8.6	0.28	2	250	1	8.4
HD 206267A	HR 8281	O6 e	5.62	99.29	+3.74	14.0	0.53	4	1000	2	8.7
HD 207198	HR 8327	O9 IIf	5.96	103.14	+6.99	13.5	0.62	4	990	2	8.8
HD 207308		B0.5 V	7.49	103.11	+6.82	13.4	0.50	7	810	2	8.7
HD 207538		O9 V	7.30	101.60	+4.67	13.6	0.64	4	840	2	8.7
HD 208266		B1 V	8.14	102.71	+4.98	13.3	0.52	7	690	2	8.7
HD 210839	$\lambda$ Cep	O6 Iab	5.09	103.83	+2.61	12.8	0.57	2	510	1	8.6

<sup>a</sup> We have used the SIMBAD database for non-photometric data.

<sup>b</sup> The correction from heliocentric velocity to the LSR frame.

<sup>c</sup> (1) Fruscione et al. 1994; (2) Valencic et al. 2004; (3) Le Coupanec at el. 1999; (4) Jensen et al. 2005; (5) Andersson et al. 2002; (6) Wegner 2003; (7) Simonson 1968.

<sup>d</sup> (1) Parallax distance from  $\geq 4\sigma$  Hipparcos results; (2) Spectroscopic parallax based on absolute magnitudes from Walborn 1972 and Walborn 1973.

TABLE 2  
HST SPECTROSCOPY OF PROGRAM STARS

Star	Data set	Grating	Slit (arcsec)	S/N	$R$
STIS Data					
HD 22951	o64805-9	E140H	0.2X0.05	105	121,000
HD 23180	o64801-4	E140H	0.2X0.05	100	119,000
HD 23478	o6lj01	E140H	0.1X0.03	50	135,000
HD 24398	o64810-11	E140H	0.2X0.05	90	121,000
HD 24534	o64812-13	E140H	0.1X0.03	105	140,000
	o66p01-02	E140H	0.2X0.09	110	101,000
HD 27778	o59s01	E140H	0.2X0.09	40	96,000
HD 99872	o6lj0i	E140H	0.1X0.03	35	139,000
HD 147683	o6lj06	E140H	0.2X0.09	30	121,000
HD 148937	o6f301	E140H	0.2X0.09	30	127,000
HD 177989	o57r03-04	E140H	0.2X0.09	75	104,000
HD 192035	o6359k	E140M	0.2X0.2	35	39,000
HD 198781	o5c049	E140H	0.2X0.2	25	85,000
HD 203374A	o6lz90	E140M	0.2X0.2	45	38,000
HD 203532	o5co1s	E140H	0.2X0.2	40	80,000
HD 206267A	o5lh09	E140H	0.1X0.03	30	140,000
HD 207198	o59s06	E140H	0.2X0.09	25	100,000
HD 207308	o63y02	E140M	0.2X0.06	60	45,000
HD 207538	o63y01	E140M	0.2X0.06	55	47,000
HD 208266	o63y03	E140M	0.2X0.06	60	45,000
HD 210839	o54304	E140H	0.1X0.03	45	160,000
GHRS Data					
HD 96675	z19w01	G160M	0.25	30	19,000
HD 154368	z3dw01	G160M	0.25	115	19,000
	z0wx01	G160M	0.25	20	19,000

TABLE 3  
EQUIVALENT WIDTHS AND COLUMN DENSITIES FOR  $^{12}\text{CO}$

Star	$v'$	$\tau < 1$	$W_\lambda$ (mÅ)	$v'$	$\tau > 1$	$W_\lambda$ (mÅ)	$N/10^{14}$ (cm $^{-2}$ )
STIS Data							
HD 22951	8	0.6	$5.0 \pm 0.2$	7	1.3	$9.3 \pm 0.2$	$1.83 \pm 0.06$
HD 23180	...	...	...	8	1.5	$15.9 \pm 0.3$	$6.78 \pm 0.14$
HD 23478	9	0.7	$9.9 \pm 0.8$	8	1.6	$18.9 \pm 0.9$	$8.05 \pm 0.52$
HD 24398	...	...	...	8	5.4	$24.8 \pm 0.4$	$17.9 \pm 0.5$
HD 24534	...	...	...	12	2.2	$12.1 \pm 0.2$	$158. \pm 4.$
HD 27778	13	0.5	$5.2 \pm 1.0$	12	1.2	$12.1 \pm 0.9$	$123. \pm 17.$
HD 99872	9	0.7	$5.5 \pm 0.6$	8	1.6	$10.2 \pm 0.8$	$4.54 \pm 0.43$
HD 147683	13	0.4	$3.8 \pm 0.8$	12	1.1	$8.8 \pm 0.9$	$80.3 \pm 12.6$
HD 148937	8	0.8	$10.2 \pm 2.5$	7	1.7	$18.6 \pm 2.9$	$3.81 \pm 0.76$
HD 177989	10	0.4	$2.4 \pm 0.8$	9	1.0	$5.2 \pm 0.6$	$4.4 \pm 1.0$
HD 192035	10	0.7	$7.1 \pm 1.6$	9	1.6	$14.4 \pm 1.9$	$13.9 \pm 2.5$
HD 198781	11	0.7	$3.6 \pm 0.8$	10	1.6	$7.1 \pm 0.5$	$16.6 \pm 2.5$
HD 203374A	11	0.7	$5.7 \pm 1.2$	10	1.6	$11.5 \pm 1.4$	$25.5 \pm 4.3$
HD 203532	12	0.5	$5.0 \pm 0.7$	11	1.1	$9.1 \pm 0.8$	$45.6 \pm 5.3$
HD 206267A	...	...	...	12	1.6	$12.3 \pm 2.1$	$134. \pm 23.$
HD 207198	11	0.6	$7.2 \pm 0.8$	10	1.4	$15.1 \pm 0.5$	$31.6 \pm 2.1$
HD 207308	12	0.9	$8.6 \pm 1.5$	11	1.9	$15.2 \pm 1.1$	$83.2 \pm 10.4$
HD 207538	11	0.5	$5.5 \pm 0.7$	10	1.1	$11.6 \pm 0.9$	$23.4 \pm 2.4$
HD 208266	13	0.6	$4.8 \pm 1.6$	12	1.7	$10.7 \pm 0.9$	$116. \pm 24.$
HD 210839	11	0.9	$5.9 \pm 0.4$	10	2.2	$11.5 \pm 0.3$	$27.5 \pm 1.3$
GHRS Data							
HD 96675	...	...	...	8	4.5	$31.0 \pm 2.9$	$20.2 \pm 3.2$
HD 154368	10	0.9	$11.9 \pm 3.1$	9	2.2	$23.5 \pm 3.5$	$26.7 \pm 5.5$

TABLE 4  
EQUIVALENT WIDTHS AND COLUMN DENSITIES FOR  $^{13}\text{CO}$

Star	$v'$	$\tau < 1$	$W_\lambda$ (mÅ)	$v'$	$\tau > 1$	$W_\lambda$ (mÅ)	$N/10^{12}$ (cm $^{-2}$ )
STIS Data							
HD 22951	2	0.2	$1.7 \pm 0.2$	...	...	...	$2.31 \pm 0.33$
HD 23180	2	0.4	$6.2 \pm 0.4$	...	...	...	$9.32 \pm 0.55$
HD 23478	4	0.8	$4.9 \pm 0.9$	3	1.2	$6.9 \pm 0.9$	$12.0 \pm 1.9$
HD 24398	3	0.9	$8.2 \pm 0.3$	2	1.0	$9.5 \pm 0.3$	$16.5 \pm 0.6$
HD 24534	9	0.5	$2.4 \pm 0.2$	8	1.0	$4.7 \pm 0.1$	$186. \pm 9.$
HD 27778	8	0.5	$4.8 \pm 0.4$	7	1.1	$9.1 \pm 0.5$	$183. \pm 12.$
HD 99872	2	0.4	$3.9 \pm 0.9$	...	...	...	$5.6 \pm 1.3$
HD 147683	8	0.3	$3.2 \pm 0.4$	7	0.6	$6.3 \pm 0.5$	$113. \pm 11.$
HD 148937	2	0.3	$4.4 \pm 1.5$	...	...	...	$6.6 \pm 2.3$
HD 177989	3	0.7	$4.4 \pm 0.5$	2	0.8	$5.2 \pm 0.5$	$8.35 \pm 0.88$
HD 192035	3	0.9	$14.0 \pm 1.9$	2	1.1	$16.4 \pm 1.7$	$27.5 \pm 3.$
HD 198781	7	0.3	$1.7 \pm 0.6$	...	...	...	$27.7 \pm 10.4$
HD 203374A	5	0.6	$6.9 \pm 1.6$	4	1.0	$11.1 \pm 1.5$	$33.3 \pm 6.1$
HD 203532	8	0.4	$2.8 \pm 0.4$	7	0.9	$5.3 \pm 0.5$	$111. \pm 12.$
HD 206267A	8	0.8	$7.9 \pm 1.3$	7	1.7	$14.0 \pm 1.8$	$322. \pm 47.$
HD 207198	7	0.3	$4.0 \pm 0.6$	...	...	...	$66.1 \pm 9.7$
HD 207308	7	0.7	$7.0 \pm 0.9$	6	1.4	$12.5 \pm 0.9$	$118. \pm 12.$
HD 207538	5	0.7	$9.9 \pm 0.8$	4	1.3	$15.8 \pm 0.7$	$45.6 \pm 2.7$
HD 208266	7	0.8	$7.8 \pm 1.0$	6	1.6	$13.7 \pm 0.8$	$138. \pm 12.$
HD 210839	7	0.3	$1.7 \pm 0.3$	...	...	...	$35.4 \pm 6.2$
GHRS Data							
HD 96675	...	...	...	3	1.3	$11.7 \pm 1.8$	$24.9 \pm 3.9$
HD 154368	5	0.7	$12.9 \pm 2.7$	4	1.2	$20.5 \pm 1.0$	$71.3 \pm 9.2$

TABLE 5  
COMPARISON OF COLUMN DENSITIES AND RATIOS WITH PUBLISHED RESULTS

Star	CO	log $N$ (cm $^{-2}$ ) and $^{12}\text{CO}/^{13}\text{CO}$ values:				
		This Paper:	Previous References:			
HD 22951	12	$14.26 \pm 0.01$	(1)	14.22		
HD 23180	12	$14.83 \pm 0.01$	(1)	14.93		
HD 24534	12	$16.20 \pm 0.01$	(2)	$16.00 \pm 0.08$	(3) $16.15 \pm 0.06$	(4) $16.01 \pm 0.09$ (5) $16.13 \pm 0.20$
HD 27778	12	$16.09 \pm 0.06$	(4)	$16.08 \pm 0.03$	(5) $16.05 \pm 0.13$	
HD 177989	12	$14.64 \pm 0.09$	(5)	$14.62 \pm 0.17$		
HD 203374A	12	$15.41 \pm 0.07$	(6)	$15.38 \pm 0.04$	(7) $15.41 \pm 0.02$	
HD 203532	12	$15.66 \pm 0.05$	(5)	$15.70 \pm 0.17$		
HD 206267A	12	$16.13 \pm 0.12$	(4)	$16.04 \pm 0.04$	(5) $16.11 \pm 0.17$	(7) $16.00 \pm 0.03$
HD 207198	12	$15.50 \pm 0.03$	(4)	$15.52 \pm 0.04$	(7) $15.42 \pm 0.02$	
HD 207308	12	$15.92 \pm 0.05$	(7)	$15.93 \pm 0.05$		
HD 207538	12	$15.37 \pm 0.04$	(7)	$15.40 \pm 0.04$		
HD 208266	12	$16.06 \pm 0.08$	(7)	$16.05 \pm 0.04$		
HD 210839	12	$15.44 \pm 0.02$	(4)	$15.46 \pm 0.06$	(5) $15.41 \pm 0.04$	(7) $15.39 \pm 0.03$
HD 24534	13	$14.27 \pm 0.02$	(2)	14.43	(3) $14.29 \pm 0.02$	(4) $14.23 \pm 0.03$ (5) $14.30 \pm 0.12$
HD 27778	13	$14.26 \pm 0.03$	(4)	$14.19 \pm 0.10$	(5) $14.28 \pm 0.08$	
HD 177989	13	$12.92 \pm 0.04$	(5)	$12.82 \pm 0.08$		
HD 203532	13	$14.05 \pm 0.08$	(5)	$13.97 \pm 0.20$		
HD 206267A	13	$14.51 \pm 0.06$	(4)	$14.39 \pm 0.03$	(5) $14.42 \pm 0.08$	
HD 207198	13	$13.82 \pm 0.06$	(4)	$13.75 \pm 0.10$		
HD 210839	13	$13.55 \pm 0.07$	(4)	$13.59 \pm 0.08$	(5) $13.70 \pm 0.10$	
HD 24534	12/13	$85 \pm 5$	(2)	37	(3) $73 \pm 12$	(4) $60 \pm 13$ (5) $68 \pm 31$
HD 27778	12/13	$67 \pm 10$	(4)	$79 \pm 12$	(5) $59 \pm 14$	
HD 177989	12/13	$53 \pm 13$	(5)	$63 \pm 25$		
HD 203532	12/13	$41 \pm 7$	(5)	$54 \pm 21$		
HD 206267A	12/13	$42 \pm 9$	(4)	$46 \pm 6$	(5) $49 \pm 15$	
HD 207198	12/13	$48 \pm 8$	(4)	$59 \pm 14$		
HD 210839	12/13	$78 \pm 14$	(4)	$74 \pm 17$	(5) $51 \pm 9$	

REFERENCES. — (1) Wannier et al. 1999; (2) Kaczmarczyk 2000; (3) Sheffer et al. 2002a; (4) Sonnentrucker et al. 2007; (5) Burgh et al. 2007; (6) Sheffer, Federman, Pan, & Andersson 2003; (7) Pan et al. 2005.

TABLE 6  
CO ISOTOPIC RATIOS AND FRACTIONATION PARAMETERS

Star	$^{12}\text{CO}/^{13}\text{CO}$	$F_{13}$	$T_{\text{kin}}$ (K)	$I_{\text{UV}}$	$\tau_{\text{UV}}$	$n_{\text{CN}}^{\text{a}}$ (cm $^{-3}$ )	$\Theta_{12}$	$\Theta_{13}$
STIS Data								
HD 22951	$79 \pm 12$	1.13	40	1.0	1.49	225	0.473	0.563
HD 23180	$73 \pm 5$	1.04	40	1.0	1.86	625	0.298	0.450
HD 23478	$67 \pm 13$	0.96	50	1.0	1.67	525	0.275	0.435
HD 24398	$108 \pm 5$	1.54	30	1.0	2.05	700	0.189	0.362
HD 24534	$85 \pm 5$	1.21	20	1.0	3.84	650	0.0372	0.154
HD 27778	$67 \pm 10$	0.96	50	0.5	2.29	$\sim 900$	0.0465	0.176
HD 99872	$81 \pm 21$	1.16	65	1.0	1.90	$\leq 200$	0.342	0.494
HD 147683	$71 \pm 13$	1.01	...	...	...	...	...	...
HD 148937	$58 \pm 23$	0.83	...	...	...	...	...	...
HD 177989	$53 \pm 13$	0.76	...	...	...	...	...	...
HD 192035	$51 \pm 10$	0.73	65	1.0	2.05	$\sim 1450$	0.221	0.386
HD 198781	$60 \pm 23$	0.86	65	1.0	3.26	750	0.217	0.396
HD 203374A	$77 \pm 19$	1.10	50	1.0	3.69	80	0.160	0.333
HD 203532	$41 \pm 7$	0.59	...	...	...	...	...	...
HD 206267A	$42 \pm 9$	0.60	50	1.0	3.13	1000	0.0372	0.154
HD 207198	$48 \pm 8$	0.69	50	1.0	3.63	130	0.128	0.290
HD 207308	$71 \pm 11$	1.01	50	1.0	3.00	550	0.0617	0.198
HD 207538	$51 \pm 6$	0.73	50	1.0	3.92	100	0.144	0.298
HD 208266	$84 \pm 19$	1.20	50	1.0	3.10	300	0.0440	0.167
HD 210839	$78 \pm 14$	1.11	50	1.0	2.36	375	0.151	0.316
GHRS Data								
HD 96675	$81 \pm 18$	1.16	50	1.0	1.58	1425	0.170	0.324
HD 147933	$125 \pm 36$	1.79	50	1.0	2.04	350	0.200	0.383
HD 148184	$117 \pm 55$	1.67	60	1.0	2.30	$\sim 300$	0.350	0.480
HD 149757	$167 \pm 25$	2.39	60	1.0	1.98	325	0.160	0.333
HD 154368	$37 \pm 8$	0.53	50	1.0	4.77	750	0.122	0.253

<sup>a</sup> Average gas density from chemical modeling, weighted by observed CN component fractions.

TABLE 7  
H<sub>2</sub>-RELATED OBSERVABLES

Star	$\log N(\text{H}_2)$ ( $\text{cm}^{-2}$ )	$T_{0,1}(\text{H}_2)$ (K)	$T_{0,4}(\text{H}_2)$ (K)	$I_{\text{UV}}^{\text{a}}$	$n_{\text{H}_2}^{\text{a}}$ ( $\text{cm}^{-3}$ )
HD 22951	20.46	63	...	...	...
HD 23180	20.61	48	...	...	...
HD 23478	20.57	55	171	...	...
HD 24398	20.67	57	$\geq 117$	...	...
HD 24534	20.94	54	152	95	1900
HD 27778	20.79	51	152	80	1230
HD 96675	20.87	55	164	...	...
HD 99872	20.51	66	179	...	...
HD 147683	20.74	58	185	...	...
HD 147933	20.57	46	...	...	...
HD 148184	20.63	46	...	...	...
HD 148937	20.71	69	228	...	...
HD 149757	20.65	54	$\geq 129$	...	...
HD 154368	21.16	46	140	...	...
HD 177989	20.15	49	198	...	...
HD 192035	20.68	68	205	1200	18400
HD 198781	20.56	65	191	570	10900
HD 203374A	20.70	76	135	17	260
HD 203532	20.70	47	169	220	2600
HD 206267A	20.86	58	156	110	1350
HD 207198	20.83	60	162	168	1900
HD 207308	20.86	57	162	...	...
HD 207538	20.91	66	145	53	610
HD 208266	[20.94] <sup>b</sup>	...	...	...	...
HD 210839	20.84	69	218	2300	33000

<sup>a</sup> Radiation field strength and gas density as implied by UV excitation of  $N_{\text{J}=4}(\text{H}_2)$ .

<sup>b</sup>  $N(\text{H}_2)$  for HD 208266 is predicted from  $N(\text{CH})$  and  $N(\text{CO})$ , see Table 2 in Pan et al. 2005.

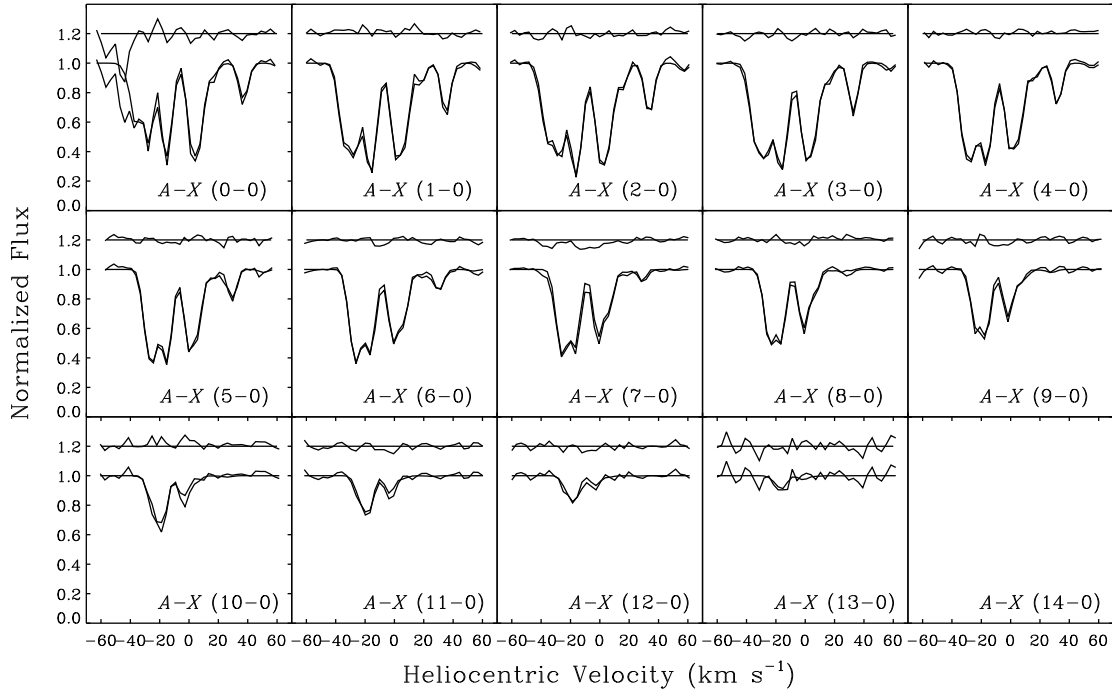


FIG. 1.— Example of a complete simultaneous fit to all 14 detectable  $A-X$  bands of  $^{12}\text{CO}$  redward of  $\text{Ly}\alpha$  along the sight line of HD 208266. This complete detection is possible thanks to the large value of  $N(^{12}\text{CO})$  and to the extensive ( $>315 \text{ \AA}$ ) coverage of the STIS E140M setup. The residual absorption on the blue side of the (0-0) band is from  $^{13}\text{CO}$ , of which eight  $A-X$  bands are modeled in Fig. 2. The noise is appreciably larger at the (13-0) band, which is  $\sim 14 \text{ \AA}$  redward of the  $\text{Ly}\alpha$  line center. The undetected (14-0) band is weaker than (13-0) by a factor of 2, and is completely lost in the noise inside the  $\text{Ly}\alpha$  core. The quality of the fit is indicated by the variation of residuals about the 1.2 level in this figure and in Fig. 2.



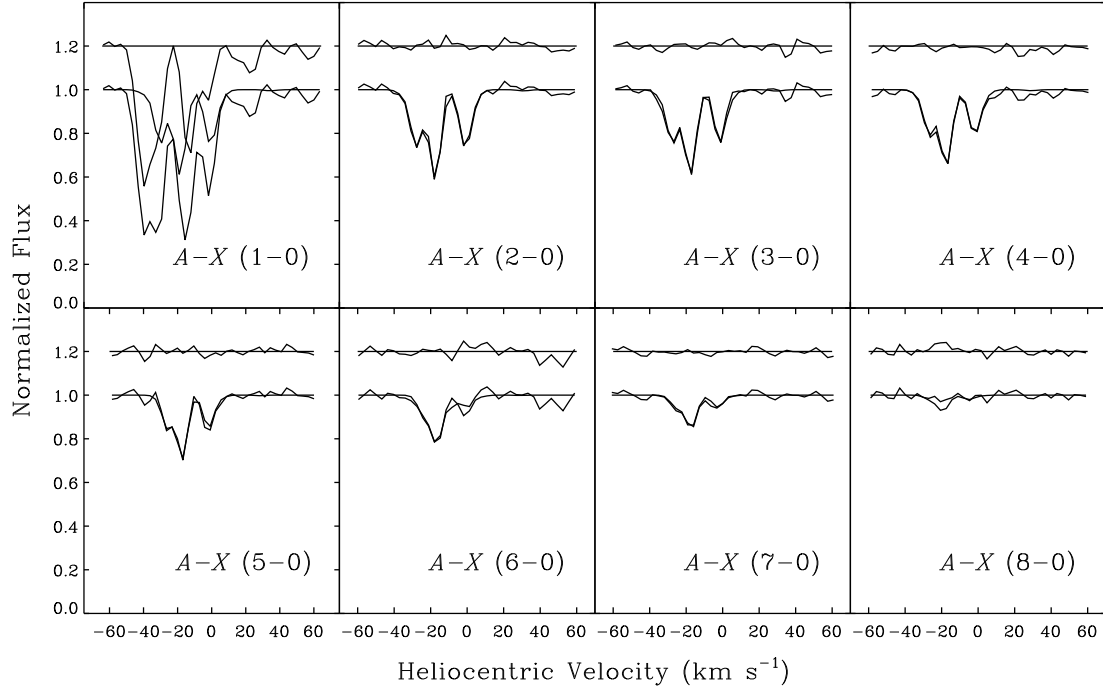


FIG. 2.— Simultaneous fit to 8  $A-X$  bands of  $^{13}\text{CO}$  for HD 208266. The prominent absorption feature blended with the (1–0) band is the  $d-X$  (5–0) band of  $^{12}\text{CO}$ , which is the strongest intersystem transition in CO. For this reason, the (1–0) band was not incorporated into the fit, yet it shows good agreement with the global model.

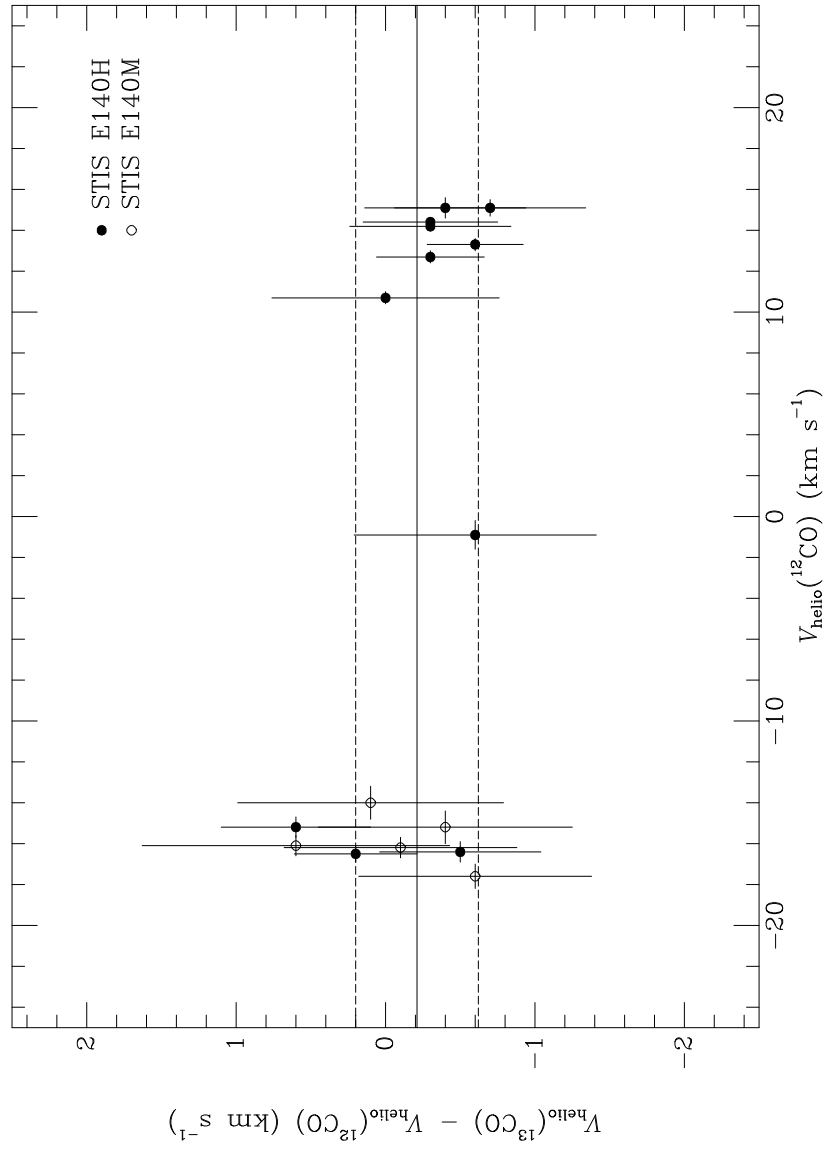


FIG. 3.— Difference in radial velocity between  $^{13}\text{CO}$  and  $^{12}\text{CO}$  for STIS sight lines shows the good agreement between the two species, and hence supports a physical association between them. No difference is seen between results from the E140H and E140M gratings. GHRs spectra have larger wavelength calibration uncertainties and their results are not plotted.

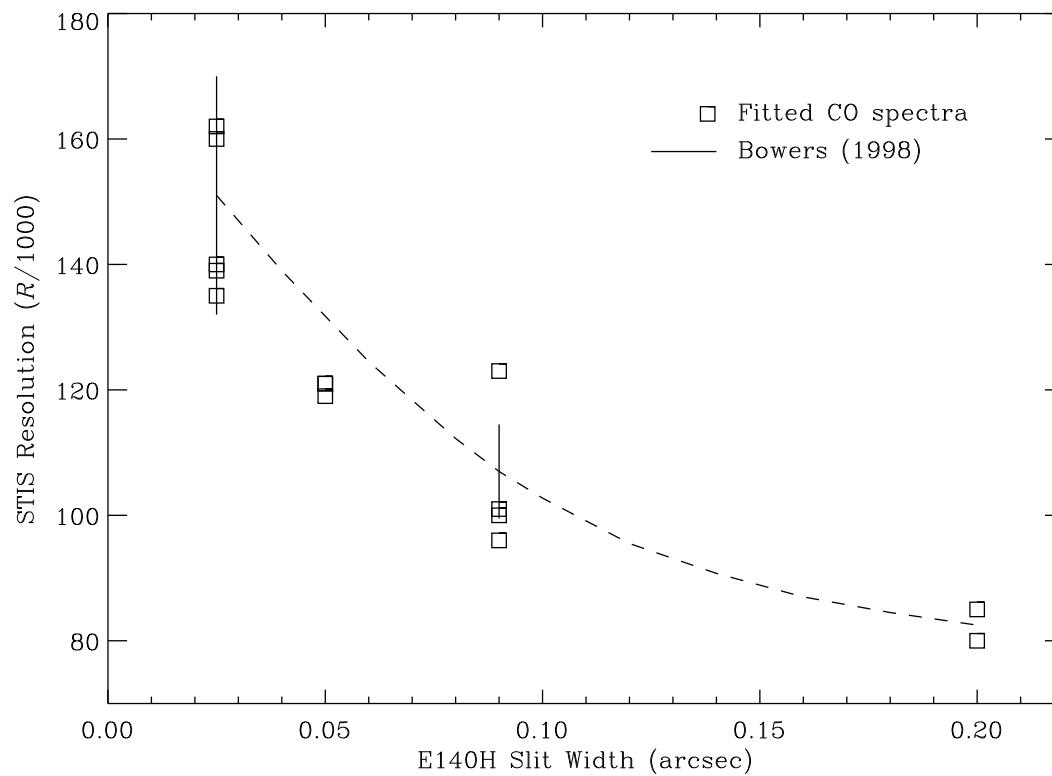


FIG. 4.— Resolving power ( $R$ ) from our fits to STIS spectra is plotted against the slit width used with the E140H grating. Note that the y-scale corresponds to the value of  $R/1000$ . A freely drawn dashed line shows the non-linear trend of  $R$  as a function of slit width. Two “error bars” show the range of results from Bowers (1998), which agree nicely with our determinations.

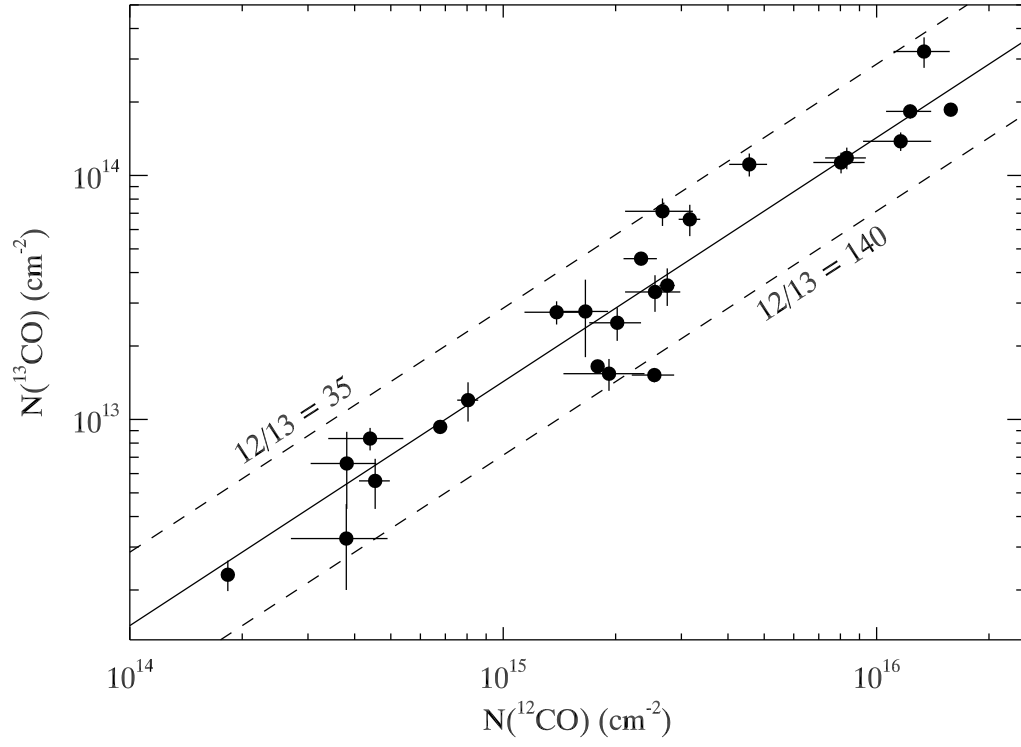


FIG. 5.— Measured column densities for both  $^{12}\text{CO}$  and  $^{13}\text{CO}$ . For comparison,  $^{12}\text{C}/^{13}\text{C} = 70$  is depicted by the solid line. Except for one sight line, 96% of the sample have fractionation values within a factor of 2 of 70, as delineated by the dashed lines corresponding to  $^{12}\text{CO}/^{13}\text{CO} = 35$  and 140, or  $F_{13} = 0.5$  and 2.0.

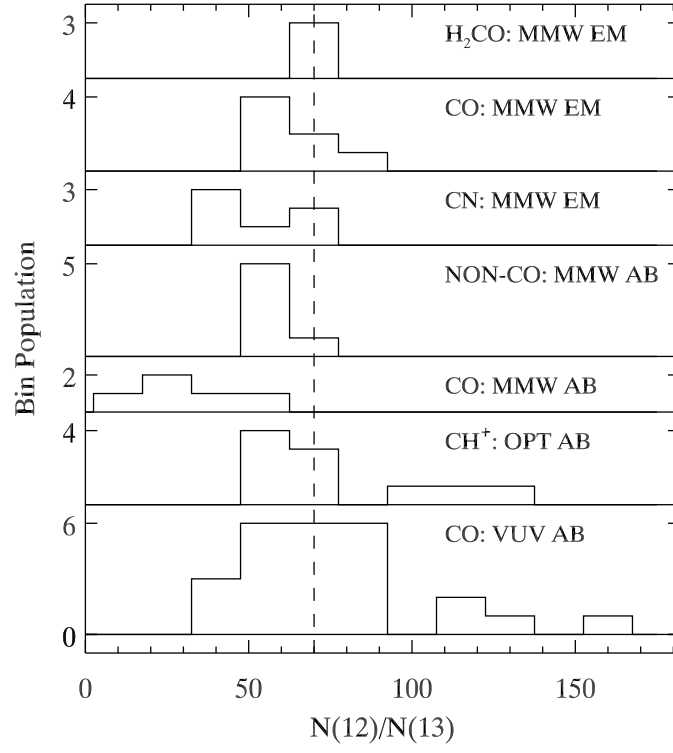


FIG. 6.— Histograms of 12-to-13 carbon ratios from absorption (ab) or emission (em) surveys conducted in various spectral regimes. A reference bin has been centered at  $70 \pm 7$ , with all other bins having the same  $2\sigma$  width.

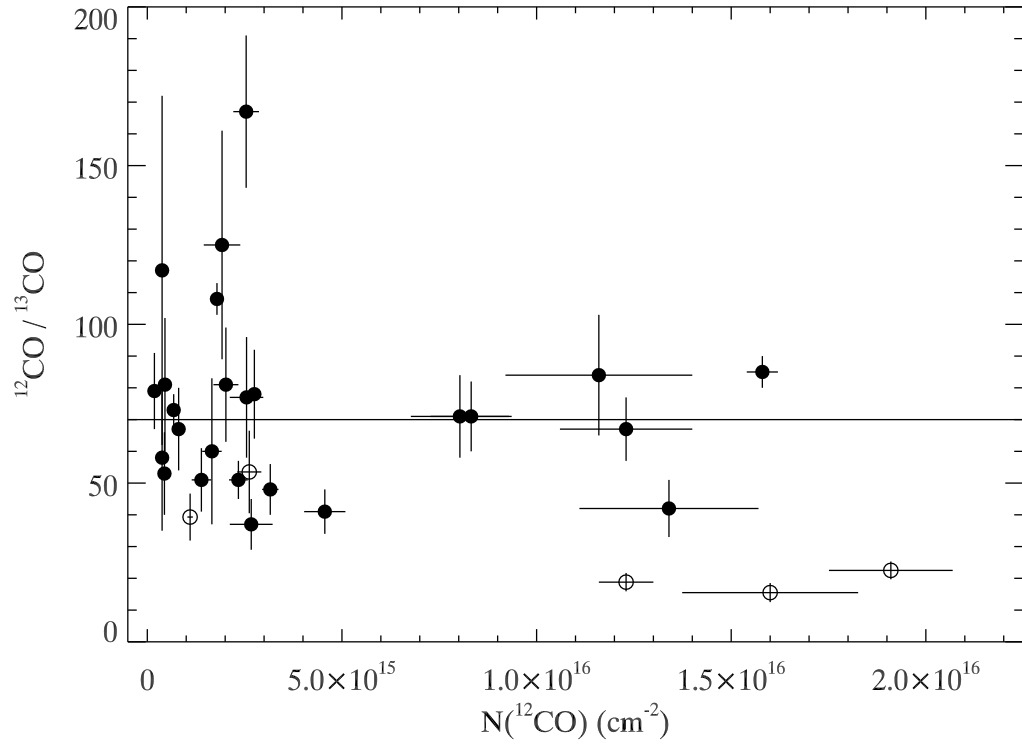


FIG. 7.— CO isotopic ratio versus column density of  $^{12}\text{CO}$ . Filled symbols denote UV determinations, while empty symbols stand for the mm-wave absorption measurements of Liszt & Lucas (1998). The CO along the latter sight lines has been summed for all velocity components for the sake of consistency with the VUV results. A solid line shows the adopted isotopic carbon ratio of 70.

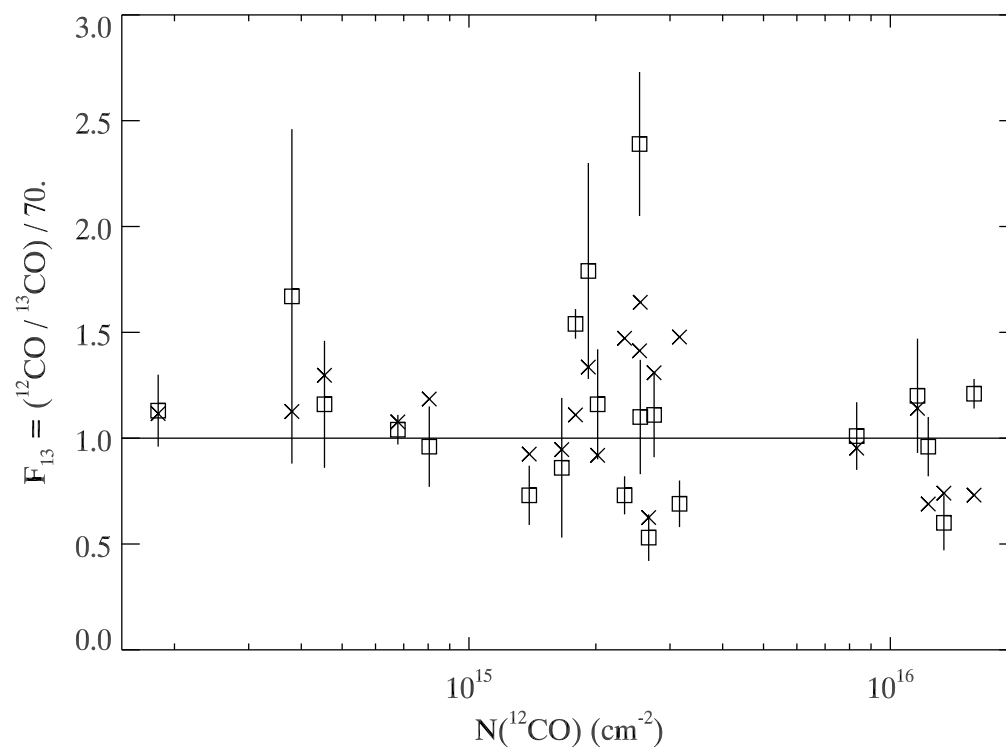


FIG. 8.— Observed CO isotopic ratios, normalized by the carbon isotopic ratio, are plotted versus  $\log N(^{12}\text{CO})$  as empty squares. A comparison is made with fractionation predictions (denoted by X symbols) based on the Lambert et al. (1994) formula and on tabulated shielding values from van Dishoeck & Black (1988).

